

# Geomagnetic Pulsations Driving Geomagnetically Induced Currents

Michael Heyns<sup>1,1</sup>, Stefan Lotz<sup>1,1</sup>, and Charles Gaunt<sup>2,2</sup>

<sup>1</sup>South African National Space Agency

<sup>2</sup>University of Cape Town

November 30, 2022

## Abstract

Geomagnetically induced currents (GICs) are driven by the geoelectric field induced by fluctuations of Earth's magnetic field. Drivers of intense GICs are often associated with large impulsive events such as coronal mass ejections. To a lesser extent fluctuations from regular oscillations of the geomagnetic field, or geomagnetic pulsations, have also been identified as possible drivers of GICs. In this work we show that these low-frequency pulsations are directly observed in measured GIC data from power networks. Due to the low-pass nature of GICs, Pc5 and lower frequency pulsations drive significant GICs for an extended duration at mid-latitudes. Longer period Ps6-type disturbances apparently not typical of mid-latitudes are seen with GIC amplitudes comparable to the peak GIC at storm sudden commencement. The quasi-ac nature of the sustained pulsation driving affects the power system response and cannot be properly modelled using only dc models. A further consideration is that the often used dB/dt GIC proxy is biased to the sampling rate of the geomagnetic field measurements used. The dB/dt metric does not adequately characterise GIC activity at frequencies in the low ULF range and a frequency weighted proxy akin to geoelectric field should be used instead.

# Geomagnetic Pulsations Driving Geomagnetically Induced Currents

M. J. Heyns<sup>1,2</sup>, S. I. Lotz<sup>1</sup>, C. T. Gaunt<sup>2</sup>

<sup>1</sup>SANSA Space Science, Hermanus

<sup>2</sup>University of Cape Town, Cape Town

## Key Points:

- Low-frequency geomagnetic pulsations couple effectively to GICs and need to be taken into account in modelling power network response
- Ps6-type disturbances along with other pulsations are seen at mid-latitudes during intense storms and can drive significant GICs
- $dB/dt$  may not be an appropriate GIC proxy given pulsation driving

---

Corresponding author: M. J. Heyns, [mheyns@sansa.org.za](mailto:mheyns@sansa.org.za)

Corresponding author: S. I. Lotz, [slotz@sansa.org.za](mailto:slotz@sansa.org.za)

## Abstract

Geomagnetically induced currents (GICs) are driven by the geoelectric field induced by fluctuations of Earth’s magnetic field. Drivers of intense GICs are often associated with large impulsive events such as coronal mass ejections. To a lesser extent fluctuations from regular oscillations of the geomagnetic field, or geomagnetic pulsations, have also been identified as possible drivers of GICs. In this work we show that these low-frequency pulsations are directly observed in measured GIC data from power networks. Due to the low-pass nature of GICs, Pc5 and lower frequency pulsations drive significant GICs for an extended duration at mid-latitudes. Longer period Ps6-type disturbances apparently not typical of mid-latitudes are seen with GIC amplitudes comparable to the peak GIC at storm sudden commencement. The quasi-ac nature of the sustained pulsation driving affects the power system response and cannot be properly modelled using only dc models. A further consideration is that the often used  $dB/dt$  GIC proxy is biased to the sampling rate of the geomagnetic field measurements used. The  $dB/dt$  metric does not adequately characterise GIC activity at frequencies in the low ULF range and a frequency weighted proxy akin to geoelectric field should be used instead.

## Plain Language Summary

Geomagnetically induced currents (GICs) are naturally occurring currents induced in conductive media, such as the Earth, by fluctuations of the geomagnetic field. When large grounded conductors such as power networks are present, these currents also enter the network and pose serious risk to the stability of the network. In extreme cases, the GICs can result in total network collapse. Particular fluctuations of the local geomagnetic field are geomagnetic pulsations, which occur when the magnetic field lines are perturbed and ring, causing oscillations. These oscillations have not previously been thought to be effective in driving large GICs, but now measured GIC data have shown this is not always the case and the power grid couples particularly well to low-frequency pulsations. Essentially, the power grid acts as an antenna and pulsations have been picked up where not previously expected. Understanding the effectiveness of these pulsations and including them in GIC modelling is vital for protection of the grounded power networks we rely on.

## 1 Introduction

Research on the occurrence of geomagnetically induced currents (GICs) in power grids is largely focused on the impact of intense sudden perturbations to the geomagnetic field (B-field) such as during sudden commencements and substorms (Kappenman, 2005; Smith et al., 2019; Freeman et al., 2019). These periods are typically characterised by spike-like peaks with large  $dB/dt$  values. Similar peaks are induced in the geoelectric field (E-field) that drives GICs. In the frequency domain, and assuming Fourier decomposition, spikes associated with extreme rates of change require broadband frequency contributions to be reproduced mathematically. GICs on the other hand have been shown to be low-frequency phenomena, with their quasi-dc nature often exploited to model network impacts by assuming pure dc driving (Lehtinen & Pirjola, 1985). Previous work based on measured GIC data in 4 different mid-latitude power systems has shown that most of the GIC power sits below 50 mHz and there is a distinct low-pass filter response (Oyedokun et al., 2020). As a result, in addition to broadband driving from impulses affecting all frequencies across B-field, E-field and GIC, low-frequency driving is very efficient in inducing GICs. A further implication for GIC modelling is that periods of low-frequency GIC from low-frequency geomagnetic driving have to be modelled exactly as such and not approximated as dc – including low-frequency driving results in a different system response (Jankee et al., 2020).

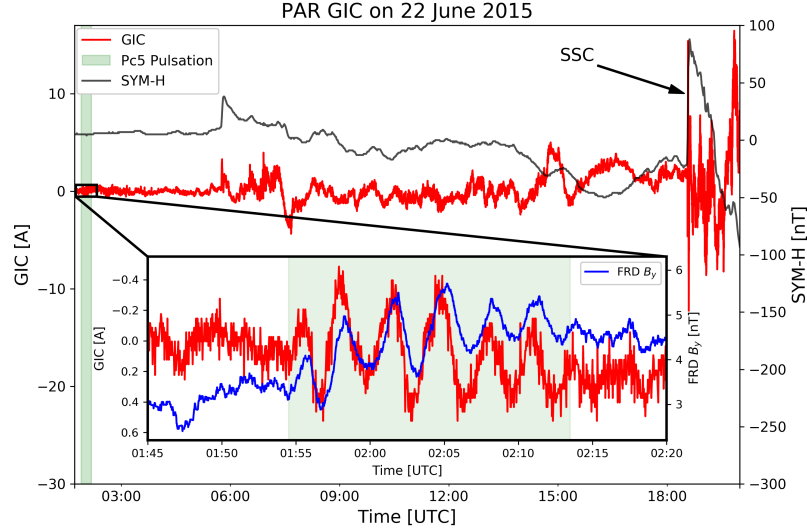


**Figure 1.** Low amplitude 5.3 mHz Pc5 pulsation (green shaded region) in the noise at PAR substation (red) in the TVA network during geomagnetically quiet time (as seen in the SYM-H index). Pc5 pulsations occur in both B-field components, with the H or  $B_x$  component contribution often larger. The effective network around PAR extends southwards and mostly the D or  $B_y$  component of the nearby FRD magnetic observatory B-field (blue) is apparent in GIC data. For scale, the storm sudden commencement (SSC) with peak GIC is shown towards the right of the main time-series. Also evident is the start of geomagnetic driving with a sudden impulse in both SYM-H and GIC data just past 06:00 UTC.

Besides sudden commencements (a typical example is seen driving large GICs on the right-hand side of Figure 1), substorms and other impulsive events are seen as main drivers of GICs. At mid-latitudes though, substorms and their magnetic bay signatures (Watari et al., 2009) do not have the sustained duration to be of concern regarding ac modelling nor the GIC maxima associated with commencements or impulses. There are also secondary drivers of GICs, which include geomagnetic pulsations (Viljanen et al., 1999; Pulkkinen et al., 2005). These oscillations of the B-field within the ultra low-frequency (ULF) band (roughly 1 mHz – 1 Hz) are of particular interest due to their sustained and low-frequency nature, being described in more detail in Section 2. Pulsation driven GICs are often disregarded in comparison to peak GICs associated with impulsive events. It has further been suggested that the rate of change due to pulsations is not extreme enough to cause large GICs (Viljanen et al., 1999). Both statements are often true, especially at mid-latitudes where the driving current system tends to be the ring current and the auroral and substorm effects are negligible in comparison (de Villiers et al., 2017). Given significant low-frequency disturbances or pulsations during intense geomagnetic storms, significant GICs could indeed result due to the effective low-pass coupling, which introduces sustained driving. An example of such coupling is seen in the Kola peninsula, where recent work has shown direct links between pulsation-like disturbances and some of the largest measured GIC values in that network (Sokolova et al., 2019; Belakhovsky et al., 2019; Kozyreva et al., 2019; Apatenkov et al., 2020). In this paper similar coupling is unexpectedly seen at mid-latitudes, with sustained moderate GICs being produced. The effects on the network of such distinctly low-frequency ac current is the subject of continued research (Jankee et al., 2020), especially when there is exposure over an extended period.

Regardless of source, the inductive coupling between  $dB/dt$  in the Earth and the E-field that drives the GIC is not linear in the time domain, with the Earth's conductivity needing to be taken into account in the frequency domain. As such, a frequency weighted  $dB/dt$  analogous to the E-field is a much better proxy to GICs than simply using  $dB/dt$ . Ultimately, it is the E-field that is used in GIC modelling and calculations (Lehtinen & Pirjola, 1985). The E-field and GIC are effectively the output of a low-pass filter of  $dB/dt$  at Earth's surface (Oyedokun et al., 2020). Thus, the coupling between B-field variation and the power grid is particularly good at lower frequencies, irrespective of amplitude. Geomagnetic pulsation intervals with periods of 1 minute (in the Pc4 band) and longer are examples of this coupling. In Figure 1, the coupling of Pc5 pulsations to GICs in the frequency domain is apparent, even though both the GIC and B-field amplitudes are very small ( $dB/dt$  around 1 nT/min at maximum). At this level of GIC exposure, no damage is expected whatsoever. What is interesting nevertheless is the extent of coupling in the frequency domain, with the low-amplitude low-frequency signal lifted out of the high-frequency noise. In other words, the power network can be thought to be more sensitive to low-frequency driving. Longer period pulsations which often have larger amplitudes and can be effective drivers of sustained and significant GICs.

The focus of this paper is on the evidence of significant pulsation driven GICs at mid-latitudes, often not identified or considered, but linking directly to ac modelling of GICs and sustained stress on the power system. Section 2 describes GIC effective pulsation phenomena further, along with the types of effects that may be seen in power networks. Section 4 analyses three storms with GIC effective pulsation events with the preceding Section 3 describing the data used. The storms covered are the 2003 Halloween Storm that initiated significant accumulated damage in the South African power network and was the largest geomagnetic storm in solar cycle 23; an apparently typical intense geomagnetic storm in June 2015 and finally the famous March 1989 Storm that led to the collapse of the Hydro-Québec power network and is now used for regulatory benchmarking (*TPL-007-1: Transmission System Planned Performance for Geomagnetic Disturbance Events*, North American Reliability Corp., 2017.). The first two storms make use of measured GIC data, whereas the last storm is the widely used benchmark geomagnetic disturbance (GMD) event for power utilities which uses derived E-field data. The benchmark event is included specifically to show that low-frequency GIC modelling of the network response is needed given the existence of GIC effective pulsations. It is further shown in Section 5 that using a proxy with incorrect frequency weighting, such as  $dB/dt$ , may not reproduce the effects of pulsations at frequencies significantly different to the sampling frequency.

## 2 Geomagnetic Pulsations and GIC Effects

Pulsations of Earth's B-field, also called geomagnetic fluctuations or oscillations, have been studied since the 1800's. As research in the field grew, a classification system developed to group similar pulsations by source, period and other general characteristics. In broad terms there are continuous pulsations (Pc1–6) which are truly periodic or sinusoidal and irregular pulsations (Pi1–3) which are quasi-periodic and often sit on magnetic bays (Saito, 1969). Within these broad pulsation classes there are further subclasses, particularly within the irregular pulsation classes. In this paper long period pulsations in GIC data are linked to geomagnetic pulsations, specifically in the Pc5 (periods of a few minutes) and Ps6 (subclass of Pi3 pulsations, with periods of tens of minutes) bands of ULF.

Pc5 pulsations (period 150 – 600 s) are 'continuous' type pulsations with durations of tens of minutes and commonly seen in the auroral oval. Various generating mechanisms exist, from global magnetospheric oscillations to more small-scale, localised sources. Shear waves due to Kelvin-Helmholtz type oscillations of the magnetospheric boundary layers, driven by high speed solar wind can cause global modes of oscillation; pressure

fluctuations in the solar wind can cause a rippling of the magnetopause, propagating waves to the inner magnetosphere where coupling to local field line resonance modes cause the surface magnetic field to fluctuate at Pc5 frequencies (Walker, 2005). Stephenson and Walker (2002) presented evidence of Pc5 band waves in the solar wind entering the magnetosphere and coupling directly to field line resonances at the appropriate L-shell. Storm time Pc5 waves generally have high amplitudes (can be more than two orders of magnitude higher than quiet time Pc5's) and global coverage (Potapov et al., 2006; Marin et al., 2014). It is these type of extreme event Pc5 pulsations that are seen at mid-latitudes, which otherwise would be constrained to Pc3 pulsations driven by field line resonances. Pilipenko et al. (2010) provides a good overview of global large amplitude Pc5 pulsations and showed that they mostly occur during storm recovery phase, driven by high speed solar wind streams in the presence of increased solar wind pressure (Marin et al., 2014). The high speed stream sets up a Kelvin-Helmholtz instability, causing magnetohydrodynamic oscillations in the global magnetospheric waveguide. During intense storms significant wave power can penetrate to low-latitude regions (Pilipenko et al., 2010). Pc5 pulsations are typically the result of the global ringing geomagnetic field lines. The gaps or cavities between field lines in the magnetosphere can act as waveguides for waves from sources internal or external to the magnetosphere. The cavity modes in turn couple to field line resonances, which oscillate at discrete frequencies (McPherron, 2005). Both horizontal B-field components are affected, but the H or  $B_x$  component (i.e. the geomagnetic or geographic north component, roughly aligned to the Earth's main field) is usually larger. In this paper focus is placed on the horizontal B-field components as we are specifically interested in GIC linked disturbances. Most GIC studies assume the incident disturbance B-field is a vertically incident plane wave locally (Viljanen et al., 2004), similar to the base assumption in traditional magnetotelluric studies (Cagniard, 1953). In such a case, the horizontal B-field components are the dominant drivers of the horizontal E-field that drives GICs. Although there are possible deviations from this assumption (Neska et al., 2018), locally at mid-latitudes the magnetospheric sources are far enough that the horizontal B-field components typically still dominate. For these horizontal Pc5 B-field pulsations global power systems are affected, with both north-south and east-west effective nodes being susceptible. East-west nodes are however more affected due to the larger  $B_x$  component contribution inducing a larger roughly orthogonal E-field.

Periods longer than Pc5 can be classified either in the general Pc6 or Pi3 bands. Pc6 pulsations are not a typical form of continuous ULF pulsations as their period is too long for any cavity mode in the magnetosphere. These pulsations are associated more with tail dynamics or fluttering. There would also be cases where periodic substorms show apparent periodicity, although the recurrence timescale is typically on the order of hours and due to the interaction between the state of the magnetosphere and solar wind driving (Borovsky & Yakymenko, 2017). A better defined class of pulsations that overlap with Pc6 pulsations are Ps6 pulsations, a subclass of the general Pi3 band. These Ps6 pulsations are long period irregular pulsations associated with substorms and with periods ranging from 5 to 40 minutes, mostly seen in the D (or  $B_y$ ) component of the B-field and originally defined in the auroral zone (Saito, 1978). Ps6 events are thought to be driven by the fluctuation and 'meandering' of the ground-based footprints of field-aligned current (FAC) systems observed during substorms. They usually occur in conjunction with so-called omega-band auroral structures at the auroral boundary (Saito, 1978; Lühr & Schlegel, 1994; Amm et al., 2005) during substorm onset (Wild et al., 2011) or recovery (Saito, 1978) phases. These ionospheric manifestations of omega-bands and Ps6 pulsations are further thought to be the end of a chain of processes starting with Earth directed flow bursts in the magnetotail (Henderson et al., 2002). Compared to the global Pc5 events, Ps6 events are distinctly different, being more localised and affecting north-south nodes in a power network due to the dominant  $B_y$  component of the B-field. The spatial localisation of these pulsations applies both in latitude and longitude, with longitude drift often seen in auroral regions (Vanhamäki et al., 2009). Large power grids

can span large areas and as such these meandering structures can move across different sections of a network, making dense B-field measurements necessary.

The link between GICs and geomagnetic pulsations has been established in previous literature, although the extent has not always been clear and has generally focused on high-latitudes. During the recovery phase of the 6–7 April 2000 geomagnetic storm, Pc5 pulsations with a period between 5 and 8 minutes were identified in the Finnish power system (Pulkkinen et al., 2003). It was noted that despite the relatively low amplitude of the GIC pulsations (33% of peak at storm sudden commencement), there is a risk of cumulative erosion in pipeline GICs. During the recovery phase of the Halloween Storm, sustained mid-latitude pulsations were noted in the USA (Kappenman, 2005) and in Czech pipelines (Hejda & Bochníček, 2005), which were also identified as Pc5 pulsations. In 10 large storms between 1999 and 2005, there were Pc5 pulsations driving GICs in the local morning or post-midnight sectors at high-latitudes during the recovery phase (Pulkkinen & Kataoka, 2006). A further study similarly looked at the difference in spectra between 32 CME (coronal mass ejection) and 3 CIR (corotating interacting region) driven storms. For CIR storms pulsations in the Pc3–5 range were seen, especially in the local day-side during the recovery phase. Smaller CME storms do not always show pulsations in the recovery phase. In the 27–28 December 2005 CIR storm, low amplitude GIC as a result of pulsations were seen at Memanbetsu, a mid-latitude site in Japan (Watari et al., 2009). More recently, long period pulsations were seen in the high-latitude Kola peninsula during the 28–29 June 2013 geomagnetic storm, producing over 120 A GIC at a particular node in the power grid (Belakhovsky et al., 2019). Pi3-type quasi-pulsations with a period of between 10 and 20 minutes resulted from a sequence of vortex-like localised structures associated with omega-bands (and Ps6 pulsations) (Apatenkov et al., 2020) embedded in a substorm bay that constructively created large GICs (Yagova et al., 2018; Belakhovsky et al., 2019; Apatenkov et al., 2020). Localised high-latitude long period Pi3 disturbances have also been noted to be dominant in the eastward B-field ( $B_y$ ) component with GIC risk in north-south effective power networks, contrary to the typical high-latitude east-west GIC driving associated with the large scale east-west auroral electrojet current system (Yagova et al., 2018). Such vortex-like current structures have also previously been related to long period morning Ps6 pulsations, which have shown correlation to particularly large  $dB/dt$  and possible GICs (Apatenkov et al., 2004). The link to fine scale disturbances, such as Ps6 pulsations, has been explicitly seen in the Kola peninsula for other events as well, with measured GICs around 25 A (Kozyreva et al., 2019).

Modern GIC risk analysis to utilities has focused largely on peak GIC values and the associated thermal damage to transformers, with a lesser emphasis on control system disruptions and harmonic production. Recently such risk analysis has been formalised with NERC, in compliance with a FERC ruling regarding the development of a geomagnetic disturbance reliability standard for utilities (*Federal Energy Regulatory Commission: Reliability Standard for Transmission System Planned Performance for Geomagnetic Disturbance Events. Order 830*, Sep 2016, Washington DC.), developing a reliability standard for utilities regarding GMD risks (*TPL-007-1: Transmission System Planned Performance for Geomagnetic Disturbance Events*, North American Reliability Corp., 2017.). This reliability standard identifies peak GIC amplitudes and thermal damage with a risk limit of 225 A in the neutral, but does not include sustained driving at lower amplitudes such as is seen during pulsation intervals. The fact that the sustained driving continues for an extended period may be significant in an accumulative damage or voltage stability sense. Such accumulated degradation may be at the heart of transformer failures in New Zealand and South Africa where the GICs in the neutral were likely not more than 19.5 and 45 A respectively, i.e. not particularly large (Divett et al., 2018; Moodley & Gaunt, 2017). Saturation for a ‘resilient’ three-phase three-limb transformer can occur with currents as low as 6 A (Gaunt & Coetzee, 2007), creating localised hotspots and bubbles in the transformer paper/oil and partial discharge (Khawaja & Blackburn,



2009) that can initiate further degradation (or accelerate existing degradation) under normal operation. The expectation is that even more damage will occur during sustained elevated driving from pulsations. Once degradation has occurred, even with oil changes, there is no reversal possible of the damaged insulation and the transformer has increasingly less resistance to future damage (Khawaja & Blackburn, 2009; Moodley & Gaunt, 2017). From that point on, the transformer is ultimately on a trajectory to premature failure. Zooming out from the transformer level, voltage stability and protection mal-operation under sustained GIC driving can create further complications and points of failure in the power system (Overbye et al., 2013; Tigere et al., 2018; Sithebe & Oyedokun, 2019). The extent of unbalance and distortion introduced by low-frequency GIC instead of dc GIC is the subject of continuing research (Jankee et al., 2020). Taking the accumulated damage viewpoint, we define/consider GIC effective pulsations as events with peak-to-peak magnitudes of 6 A or higher and/or an extended duration of multiple cycles over a period of minutes.

### 3 Data and Processing

Pulsation events are selected from three intense geomagnetic storms, defined as storms when the *Dst* (or higher resolution SYM-H) minimum is less than -100 nT (Gonzalez et al., 1994; Wanliss & Showalter, 2006). Table 1 summarises the events, locations and the types of data used.

For Events 1 and 2, or the 2003 Halloween Storm and June 2015 storm respectively, there are measured mid-latitude GIC data in which significant pulsation driving is evident. Event 1 makes use of GIC data from the Eskom network in South Africa and Event 2 uses data from the Tennessee Valley Authority (TVA) network in the USA. These events also make use of a range of INTERMAGNET ([www.intermagnet.org](http://www.intermagnet.org)) B-field measurements at the best cadence available in each case. The June 2015 storm also overlaps with local raw B-field data from the USArray Transportable Array sites RES46 and TNV47 (<http://dx.doi.org/10.7914/SN/EM>) which are used for lag estimation.

In Event 3, which is the Hydro-Québec March 1989 Storm, the induced E-field is derived from B-field measurements ( $B_x$  and  $B_y$ ) and used as proxy for GIC as no utility data was available for this event. In general, the E-field can be related to the B-field in the frequency domain through the surface impedance tensor defined by the general magnetotelluric equation,

$$\begin{bmatrix} E_x(f) \\ E_y(f) \end{bmatrix} = \begin{bmatrix} Z_{xx}(f) & Z_{xy}(f) \\ Z_{yx}(f) & Z_{yy}(f) \end{bmatrix} \begin{bmatrix} B_x(f) \\ B_y(f) \end{bmatrix}. \quad (1)$$

Given a 1D or layered-Earth, which gives a good first order approximation,  $Z_{xx}(f) = Z_{yy}(f) = 0$  and  $Z_{xy}(f) = -Z_{yx}(f) = Z(f)$  (Cagniard, 1953). The B-field and hence E-field field associated with Event 3 is the 10 s cadence benchmark profile used to inform utility GIC modelling, as defined by the North American Electric Reliability Corporation (NERC) (*TPL-007-1: Transmission System Planned Performance for Geomagnetic Disturbance Events*, North American Reliability Corp., 2017.). The B-field was measured at NRCan’s Ottawa (OTT) geomagnetic observatory and the generally well used and understood resistive Québec Earth model was used to derive the benchmark E-field (Boteler, 2015). This layered-Earth conductivity model has layer thicknesses (from top to bottom) of [15, 10, 125, 200] km, with corresponding resistivities of [20000, 200, 1000, 100]  $\Omega\text{m}$  and a half-space resistivity of 3  $\Omega\text{m}$ . The resistivities in turn define the 1D surface impedance  $Z(f)$ .

To ensure that periods exhibiting pulsation characteristics in GIC (or geoelectric) data are in fact associated with geomagnetic pulsations, there have to be similar characteristics in the B-field data, i.e. period and duration. Common characteristics across



**Table 1.** Stations and data used in analysis of GIC effective pulsation events. Geomagnetic co-ordinates are given as at date and using a quasi-dipole approximation.

Event	Date	Type	Station (Abbr.)	Data	Geog. Lat.	Geog. Lon.	Geom. MLat.	Geom. MLon.	Cadence
1	31/10/2003	Pc4	Grassridge	GIC	-33.7°	25.6°	-42.3°	90.1°	2 s
		Pc5	(GRS) Hermanus (HER)	$B_{x,y}$	-34.4°	19.2°	-42.6°	83.3°	60 s
2	23/06/2015	Ps6	Paradise	GIC	37.3°	-87.0°	47.4°	-13.8°	2 s
			(PAR)						
			St John's	$B_{x,y}$	47.6°	-52.7°	51.6°	31.5°	1 s
			(STJ)						
			Ottawa	$B_{x,y}$	45.4°	-75.6°	54.6°	2.9°	1 s
			(OTT)						
			Fredericksburg	$B_{x,y}$	38.2°	-77.4°	47.8°	-0.2°	1 s
			(FRD)						
			RES46	$B_{x,y}$	37.5°	-87.6°	47.6°	-14.6°	1 s
			(RES)						
			TNV47	$B_{x,y}$	35.4°	-87.5°	45.6°	-14.5°	1 s
			(TNV)						
3	15/03/1989	Pc5	Stennis Space Center (BSL)	$B_{x,y}$	30.4°	-89.6°	40.5°	-17.5°	1 s
			Port Stanley	$B_{x,y}$	-51.7°	-57.9°	-39.2°	10.9°	60 s
			(PST)						
			King Edward Point (KEP)	$B_{x,y}$	-54.3°	-36.5°	-45.3°	25.7°	60 s
			Orcadas	$B_{x,y}$	-60.7°	-44.7°	-48.7°	20.4°	60 s
			(ORC)						
			Argentine Islands (AIA)	$B_{x,y}$	-65.3°	-64.3°	-50.9°	9.6°	60 s
3	15/03/1989	Pc5	Ottawa (OTT)	$B_{x,y}$	45.4°	-75.6°	56.7°	0.0°	10 s

datasets rules out that the effects seen are in the measured GIC alone or due to the network or interference. GIC (or E-field) data are compared with B-field measurements in the frequency domain to ensure that oscillations of the same period are seen at the same time in both signals and are coherent. The sampling cadence is fine enough and disturbances long enough that the well defined and finite pulsation signatures are not a product of measurement noise or chance.

During the three selected geomagnetic storms, various processes result in different signatures in the horizontal B-field. The superposition of these signatures complicates the detection of pulsation waveforms. Pulsation signature detection is done by taking a rolling FFT of each signal and pre-whitening. Pre-whitening is done by normalising the spectrum according to frequency dependant baseline noise, found by fitting a linear trend in log-space of the power spectrum. To ensure the resulting spectral peaks are significant, significance levels of 5 sigma above the mean power are required for all signals (B-field and GIC/E-field) concurrently. In short, this is a band-agnostic pulsation detection process that does not rely on passing only a specific band of interest.

At this point it should also be noted that all GIC modelling and analysis depends on the network. Network effective directionality has a large part to play in modulating the effectiveness of disturbances and the influence of E-field or B-field components. Ultimately, coupling between the induced E-field and GIC is inversely related to the angle between the E-field vector and the line (Zheng et al., 2013). The network effective directionality in this case refers to the total network weighted orientation that takes into account the wider network-connected region and can be estimated through empirical network parameters. In this paper, only measured GIC data are used and no GIC modelling is done. In some cases, for example the inset of Figure 1, the sign of the measured GIC is inverted to clarify the relation to other parameters since GIC polarity is purely a result the Hall-effect sensor set-up in relation to the structure of the network. For the two measurement sites used in this paper, the sensor set-up is opposite. Network analysis of the TVA network in the USA suggests all nodes take positive GIC as being out of the ground, whereas the Eskom data in South Africa takes positive GIC as into the ground. Both nodes are effectively north-south aligned, with the implication that the north-south E-field would drive GICs. In the TVA network, the majority of the local network lies to the south of the PAR node used, and hence a northward E-field ( $E_x$ ) will produce GICs that ground and are recorded as negative GICs. In South Africa, the majority of the local network is north of the GRS node used, and a southward E-field ( $-E_x$ ) will produce GICs that ground and are recorded as positive GICs. Empirically, the network parameters scaling the northward E-field to measured GIC in both cases are negative, i.e.  $GIC \propto -E_x$ . Taking this one step further, in general terms and using the magnetotelluric equation for a 1D or layered-Earth conductivity, the northward E-field component  $E_x$  is related to orthogonal the eastward component of the B-field  $B_y$  though the surface impedance  $Z(f)$ , or  $E_x(f) = Z(f)B_y(f)$ . The  $E_y$  and  $B_x$  components are similarly related, but out of phase, i.e.  $E_y(f) = -Z(f)B_x(f)$ . Since we are only concerned with a north-south effective power network in this paper, given a dominant frequency the measured GIC can be loosely related to the single B-field component in the time domain given the network parameter polarity, i.e.  $GIC \propto -B_y$ , justifying the inverted axis in plots where pulsations are evident.

#### 4 Analysis of GIC Effective Pulsation Events

In this Section we describe three events with a number of intense GIC effective pulsation intervals. For most of these events, there have been associated GIC studies, but not in terms of pulsation driving.

#### 4.1 Event 1: 2003 Halloween Storm

During the well known Halloween Storm of 2003, the biggest of solar cycle 23, consecutive CMEs resulted in a superstorm with known damage to power grids at mid-latitudes (Gaunt & Coetzee, 2007). Figure 2 shows GIC exposure at the GRS substation in South Africa during the storm, along with the SYM-H index and a number of intense pulsation intervals. High-latitude networks also experienced faults, e.g. a low-set overcurrent relay in Malmö experienced tripping as a result of harmonics during the main phase of the storm on 30 October (Pulkkinen et al., 2005).

On 29 October, during the main phase of the first storm, GIC data showed pulsations at mid-latitudes in the North American power grid (Kappenman, 2005) and in Czech pipelines (Hejda & Bochníček, 2005). During the storm recovery phase on 31 October, further Pc5 pulsations were seen in the mid-latitude Czech pipelines. According to Sakurai and Tonegawa (2005) these Pc5 pulsations were some of the largest ever recorded in the Pc5 band.

The global pulsations identified in the recovery phases of the consecutive storms were found to have more complicated drivers than typical pulsations, with the disturbed solar wind having a large effect (Pilipenko et al., 2010; Marin et al., 2014). These global, storm time, intense Pc5 events can be seen at fairly low-latitudes and in particular in the morning and evening flanks (Pilipenko et al., 2010). At mid-latitudes all local time sectors were affected, with the largest disturbances of up to 150 nT seen in the pre-noon or noon sectors (Potapov et al., 2006). The solar wind driven pulsation periods were also confirmed in satellite data, with further analysis of Pc3 pulsation transition at the plasmasphere boundary (Balasis et al., 2015). During the periods of 05:37 to 07:40 UTC and 11:00 to 14:00 UTC on 31 October, large amplitude Pc5 pulsations were identified in Andenes (high-latitude station in Norway) and Iriomote (low-latitude station in Japan) (Sakurai & Tonegawa, 2005).

In South Africa, GIC and B-field data show intense Pc5 pulsation activity from 05:37 to 07:40 and 11:00 to 14:00 UTC (partially shown in the shaded regions of Figure 2); these are the same extreme pulsations periods discussed by Sakurai and Tonegawa (2005). During the 2 to 3 hours of pulsation driving, amplitudes of up to 65% of the peak GIC measured near storm sudden commencement (SSC) were seen. GRS, where the GIC measurements were made, is a north-south effective node and driven mainly by the weaker  $B_y$  component of the Pc5 pulsation. Of the two Pc5 pulsation intervals shown, the first between 05:37 and 06:40 has a slightly longer period of around 295 s compared to the second between 11:00 and 12:00 with a period of around 255 s. This first interval shows larger amplitude B-field oscillations and GICs. Given an east-west node, which is driven by the stronger  $B_x$  component, the associated E-field would be larger. This possibly occurred at the Matimba power station in the north of South Africa where significant accumulated damage of transformer insulation was recorded as a result of the Halloween Storm (Gaunt & Coetzee, 2007). Further analysis of magnetometer data between 04:30 and 09:30 at the Hartebeeshoek and Tsumeb INTERMAGNET stations, in the north of South Africa and Namibia respectively, show comparable or marginally larger B-field pulsation amplitudes at the low-latitude stations compared to HER, i.e. the global Pc5 pulsations penetrated to around 30° geomagnetic latitude in the Southern Hemisphere without a loss of power. This diverges from the typical view of Pc5 amplitudes decreasing with latitude (Saito, 1969) and the extent of penetration of global Pc5 pulsations seen in the Northern Hemisphere for the same event (Pilipenko et al., 2010). Across all stations, the pulsations in the  $B_x$  component were larger than the  $B_y$  component.

Also of interest are the localised Pc4 pulsations embedded on a magnetic bay (and hence multiplying their effect) with periods just short of 2 minutes unresolved in magnetic field data but seen in GRS GIC data between 00:15 and 00:45 UTC (also shown in Figure 2). The Pc4 pulsations aren't seen in the B-field due to 1 minute B-field sam-

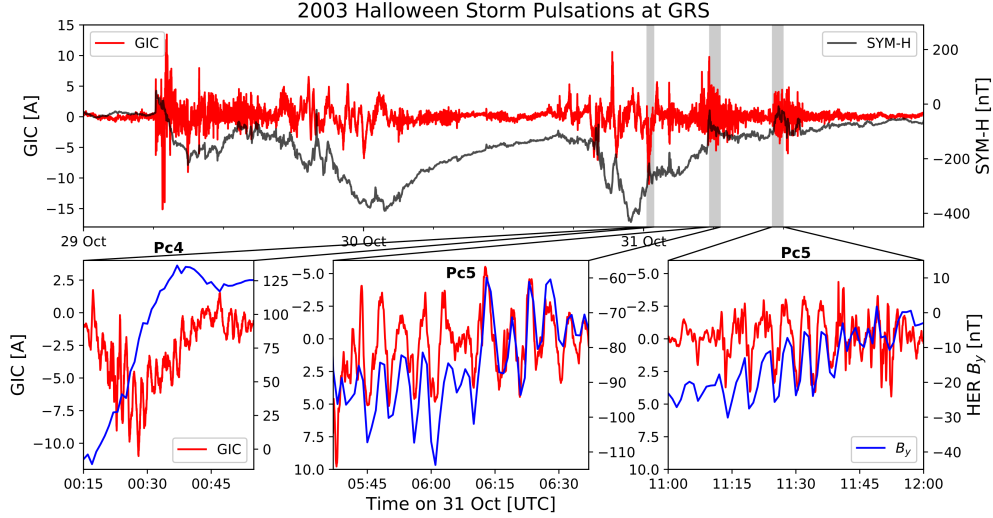


**Figure 2.** Various pulsations seen in GRS GIC data (red) during recovery phase of the 2003 Halloween Storm. Also shown is the  $B_y$  component at HER (blue), which would link to a north-south effective grid such as at GRS. Left subfigure shows Pc4 pulsations not resolved by 1 minute B-field data. Middle and right subfigures are part of previously defined periods of extreme amplitude global Pc5 pulsations (Sakurai & Tonegawa, 2005).

pling with a Nyquist frequency of 8.3 mHz not fulfilling the Nyquist criterion for 8.8 mHz pulsations. Data from local induction pulsation magnetometers at HER and Sutherland ( $-32.38^\circ$  S,  $20.81^\circ$  E), operated by the South African National Space Agency, confirm the presence of these Pc4 pulsations in the B-field at 1 s cadence.

## 4.2 Event 2: June 2015 Storm

On 22 June 2015, the arrival of a CME triggered an intense, but not extreme, geomagnetic storm (SSC at 18:33 UTC which is seen in more detail in Figure 1) with a minimum SYM-H of -208 nT reached around 04:30 UTC (seen in Figure 3). In contrast to the relatively rare Halloween superstorm, this storm can be classified as just within the threshold of a great geomagnetic storm ( $Dst \leq 200$  nT) (Le et al., 2012). On average there were 13 such storms per solar cycle between 1957–2018 (six cycles). During this particular event, significant GIC was recorded at the PAR substation in the Tennessee Valley Authority (TVA) network, south-eastern USA. Figure 3 shows the span of the storm in terms of GIC exposure and the SYM-H index in the top panel. Lower panels emphasize the interval around pulsation driving. The second shows solar wind parameters, which include a stable elevated solar wind speed and negative IMF  $B_z$  component for the duration of the Ps6 disturbance. The third panel shows the SML and SMU indices, relating to the westward and eastward electrojets respectively and indicative of substorm activity. Panels 4–7 are all ground magnetometer measurements and panel 8 is a zoomed in view of measured GIC exposure at PAR. The shaded regions are used for comparisons of cumulative driving during different phases of the storm. A peak absolute value of 16.46 A was reached within two hours after the SSC and further oscillations with peaks between 7 and 14 A (peak-to-peak variations of between 14 and 28 A) occurred near the minimum of the storm. Storm minimum occurred pre-midnight (22:43 MLT) in the TVA network and was bookended by two major substorms with expansion phases at about 03:16 and 05:09 UTC (Nakamura et al., 2016), seen as dotted lines in Figure 3. Coinciding with the substorm expansion phase are Pi2 pulsations, which are typically used

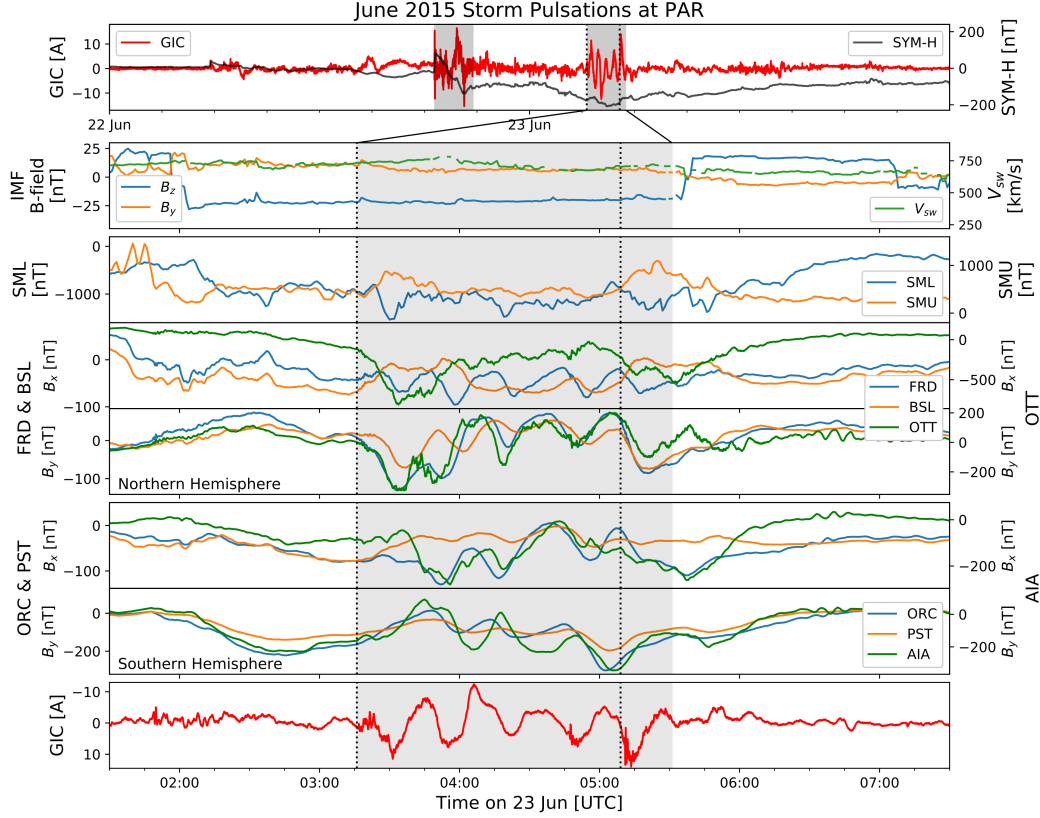


**Figure 3.** Ps6-type disturbance of roughly 23 minute periodicity as measured in GIC data at PAR in the TVA network (bottom panel), coinciding with the peak of the main phase of the geomagnetic storm (top panel). Also shown are IMF  $B_z$  and  $B_y$  components, the solar wind speed, the SuperMag SML and SMU electrojet indices (Newell & Gjerloev, 2011) and  $B_y$  component at nearby stations and conjugate stations in the Southern Hemisphere. Dotted lines indicate substorm expansion phases (Nakamura et al., 2016), coinciding with Pi2 pulsations that are often associated with substorm onset (Meng & Liou, 2004) and seen clearly in the GIC data. To compare relative GIC exposure, the second shaded region in the top panel with pulsation driving is over 10% larger than typical SSC and main phase driving of the same duration in the first shaded region.

to define substorm onset (Meng & Liou, 2004). Interestingly, these pulsations are clearly seen in the GIC data, following closely on the substorm onsets indicated by dotted lines. During the time between the two substorms that high amplitude oscillations with period of around 23 minutes are observed in the B-field across eastern North America and in the PAR GIC data shown here. Particle precipitation and currents associated with these substorms resulted in a strong westward electrojet (seen in the SML index (Newell & Gjerloev, 2011)), FACs of around 6–7 MA (Nakamura et al., 2016) and equatorward travelling ionospheric disturbances (Ngwira et al., 2019). As the storm was reaching its peak, the equatorward edge of the auroral oval as estimated by the SSUSI measurements (Paxton et al., 1992, 1993, 2017) was around  $53^\circ$  geomagnetic latitude and centred around the longitudinal region of interest (see Figure 4).

Regular long period oscillations in the B-field field over widespread regions in the midnight sector are reminiscent of the low-frequency (4–40 minute period) Ps6 disturbances that usually occur in conjunction with omega-band auroral structures (Saito, 1978;

Lühr & Schlegel, 1994; Amm et al., 2005; Apatenkov et al., 2020) near substorm onset (Wild et al., 2011; Connors et al., 2003) or recovery (Saito, 1978; Amm et al., 2005) phases. When the magnetotail snaps back to Earth, the Earthward fast flow may drive Ps6 type disturbances (Cheng et al., 2014; Henderson et al., 2002). Some authors prefer the term disturbance because these are not pulsations in the sense that they are rather the ground signatures of field-aligned current systems (Lühr & Schlegel, 1994; Amm et al., 2005). Magnetic conjugacy between hemispheres is expected, although slight asymmetry may be seen due to the small but non-zero IMF  $B_y$  component. The conjugacy is seen in the ground observations of the B-field in Northern and Southern Hemispheres shown in Figure 3. Specifically, panels 4 and 5 of Figure 3 show the B-field at magnetic observatories around PAR substation in the Northern Hemisphere. Fluctuations in the B-field are seen with a 23 minute period at all these stations, especially in the D or  $B_y$  components (which is characteristic of Ps6 (Saito, 1978; Connors et al., 2003)), out-of-phase with the GIC oscillations at PAR (bottom panel of Figure 3). At OTT, to the far northeast of PAR, the  $B_x$  component is much more susceptible to the auroral electrojet with substorm signatures evident and drowning out smaller disturbances. All magnetometers where the Ps6-type signature is seen, stretching from STJ to BSL, are further listed in Table 1 and shown in Figure 4. In panels 6 and 7 of Figure 3, Southern Hemisphere stations show similar  $B_y$  pulsation signatures, but in this case out-of-phase with their Northern Hemisphere counterparts as expected (Connors et al., 2003). The conjugacy between hemispheres allows probing of the auroral structure as seen from the SSUSI instrument aboard the sun-synchronous DMSP satellites. For this event, there was good coverage of the Southern Hemisphere as seen in Figure 4. Specifically of interest is the southern section of the F16 and F17 orbits, where an auroral bulge is seen along with auroral streamers and omega-bands. For reference AIA, ORC and PST sit at around 00:04, 00:48 and 00:10 MLT respectively. For the same orbit sections OTT, FRD and BSL sit around 23:38, 23:25 and 22:16 MLT respectively.

In general, Ps6 disturbances are thought to exhibit sunward drift (Saito, 1978), with the more common post-midnight sector disturbances associated with omega-bands having eastward drift of between 0.4 and 2 km/s (Vanhamäki et al., 2009). In the case of a pre-midnight substorm, it has been suggested that Ps6 disturbances may be associated with the westward electrojet resulting from the substorm current wedge and exhibit westward drift (Saito, 1978). Similarities in the structure of intensifications in the westward electrojet SML index support this link. Making use of B-field data from the Earth-Scope USArray magnetotelluric sites RES46 and TNV47 that coincided with this event, temporal lags in the pulsation signature between sites can be estimated. Site RES46, which is at almost exactly the same geomagnetic latitude as FRD shows a statistically significant lag of  $294 \pm 42$  s (95% confidence interval) between corresponding peaks and troughs of the pulsation signature. For this analysis, only  $B_y$  is used and peaks or troughs directly following substorm activity are ignored. The resulting lag results in what would be a rather high drift speed ( $3.98 \pm 0.61$  km/s) not typical of Ps6 disturbances. Loosely the lag estimated links with what is seen between stations in general, i.e. all westward stations lag behind eastern counterparts. From an operational GIC modelling perspective, lags of this length would introduce significant errors when using remote B-field measurements as is often done at mid-latitudes (Ngwira et al., 2009). Looking at a north-south pair of either OTT and FRD, or RES46 and TNV47, there is no statistically significant lag nor change in period of pulsations. Although the possibility of westward drift is not typical for omega-bands, the Ps6 signal at OTT suggests a mix of clockwise and anti-clockwise polarisation, as seen later through equivalent currents in Figure 5, which is typical of central or equator-side pre-midnight Ps6 disturbances in auroral regions (Saito, 1978).

Ps6 events are generally well known, having also recently been seen in GIC data (Kozyreva et al., 2019; Apatenkov et al., 2020), but it has largely been thought that they are restricted to high-latitudes. Why this average storm in particular is so effective at



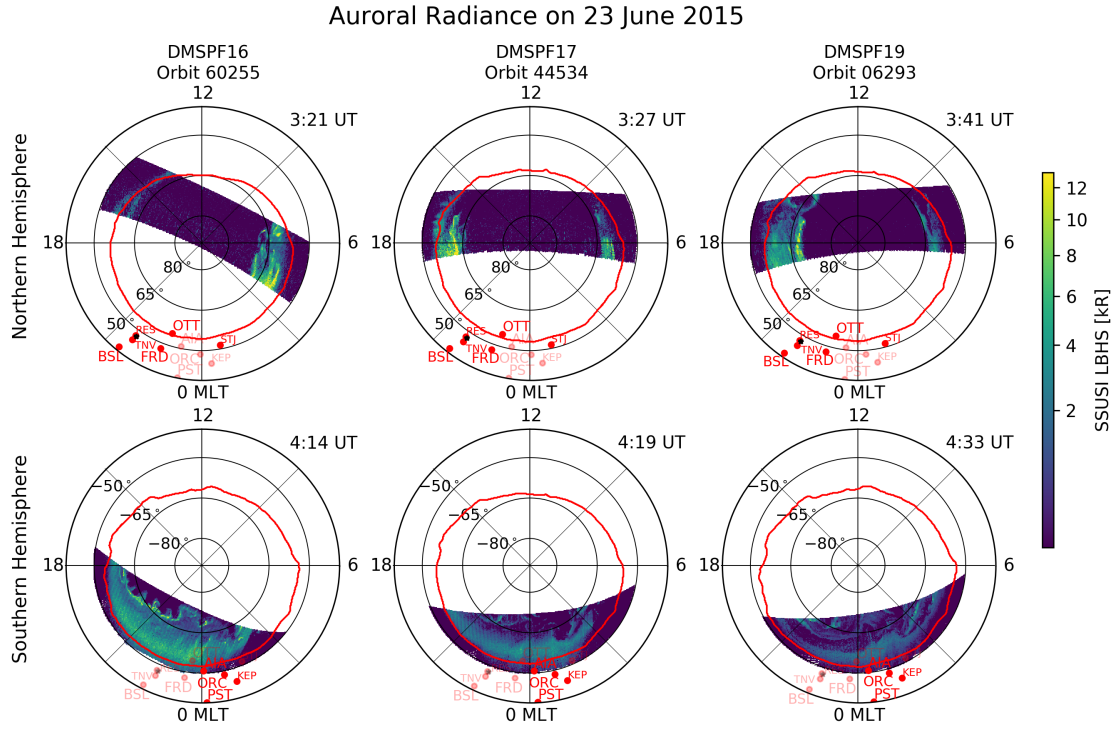


**Figure 4.** Auroral radiance in the LBH Short band from the SSUSI (<https://ssusi.jhuapl.edu/>) instrument aboard the DMSP satellites during Event 2. The equatorward boundary of the aurora as determined by the GUVI model is shown in red. The passes over Southern Hemisphere in this case include the longitudinal regions of interest. Also indicated are all the magnetometers where the Ps6-type signature was seen. Conjugate stations are faded out and the site of GIC measurements is represented by a star.



mid-latitudes is still an open question. It is most likely that multiple factors work together. Strong ionospheric electric fields are seen to add to the Ps6 driving (Connors et al., 2003), along with increased ionospheric conductivity seen during the summer solstice (June in the Northern Hemisphere as observed) (Rostoker & Barichello, 1980). The equatorward expansion of the auroral oval at the peak of a geomagnetic storm allows particle precipitation at lower latitudes. The more typical Ps6 event observed in GIC data in the Kola peninsula, which produced GICs of 25 A, also has a significantly shorter period (Kozyreva et al., 2019). Perhaps more likely is that the observed mid-latitude disturbances are a manifestation of the FACs, similar to those associated with omega-band structures in the auroral region. Apatenkov et al. (2020) recently presented a rigorous study of the omega-band driving of the extreme Pi3/Ps6 disturbances in the Kola peninsula which produced the largest GICs seen in that region. This is the same event which had previously been associated with localised current vortices (Belakhovsky et al., 2019). These current vortices are FACs that are associated with omega-bands, each omega-band having a pair of upward and downward FACs (Amm et al., 2005; Wild et al., 2000; Lühr & Schlegel, 1994). Using the approach of equivalent current vectors to estimate ionospheric Hall currents from the B-field, we can get an idea of the FAC structure associated with omega-band vortices (Lühr & Schlegel, 1994; Wild et al., 2000). Assuming an E-region sheet current greater in extent than the height of the E-region, then directly above the magnetometer we have the equivalent current components  $J_{x,y}$  given by,

$$J_x = -\frac{2}{\mu_0}\Delta B_y \quad \text{and} \quad J_y = \frac{2}{\mu_0}\Delta B_x, \quad (2)$$

where  $J_{x,y}$  is in A/m,  $\Delta B_{x,y}$  is the disturbance field in nT and  $\mu_0$  is  $4\pi \times 10^{-7}$  nT/(A/m). The equivalent currents derived may estimate overhead Hall currents but provide limited information about FACs above the ionosphere, assuming a uniformly conducting ionosphere and FACs perpendicular to the ground (Fukushima, 1976). The disturbance B-field is estimated through a first-order high-pass Butterworth filter with a cut-off period of 30 minutes to include all variation from the pulsation. Even though OTT in this case is at the equatorward boundary of the aurora and that auroral electrojet evidently affects OTT (particularly in  $B_x$  component) dampening finer scale FAC features, there are a number of characteristics that can be inferred. Given that a downward FAC has an associated clockwise Hall current and an upward FAC has an anti-clockwise Hall current, between FAC current pairs there are either strong poleward or equatorward equivalent currents, depending of the order of the pair. Such cases are seen which may suggest FAC structure, but the polarisation is not well defined and the motion or location of these structures is inconclusive. At the lower latitudes, it is not expected that the B-field disturbances are driven by overhead Hall currents. Using a similar approach though, disturbance B-field vectors are shown for FRD and ORC, which are at a similar geomagnetic latitude in the Northern and Southern Hemispheres, in Figure 5. The mid-latitude B-field disturbances in this case may include effects from weak Hall currents a distance away and the FACs themselves, which are no longer assumed to be perpendicular to the ground. The responses at these sites are much better defined, with consistent polarity. Looking at the FRD vectors, it is evident that they rotate in an anti-clockwise direction, besides at substorm onset. For a westward drifting system this suggests a driving current system poleward of FRD. For ORC in the Southern Hemisphere, the vectors rotate in a clockwise direction, also suggesting a poleward current system. Although Ps6 disturbances are often associated with omega-bands, such a link cannot conclusively be made here. However, omega-bands are not the only drivers of Ps6-like disturbances, with other FAC structures resulting in similar ground signatures (Ohtani et al., 1994). A more detailed analysis of the current event would be needed to confirm the exact driver. Regardless of driver, such low-frequency driving couples exceedingly well to GICs and can arise from seemingly average geomagnetic storms.

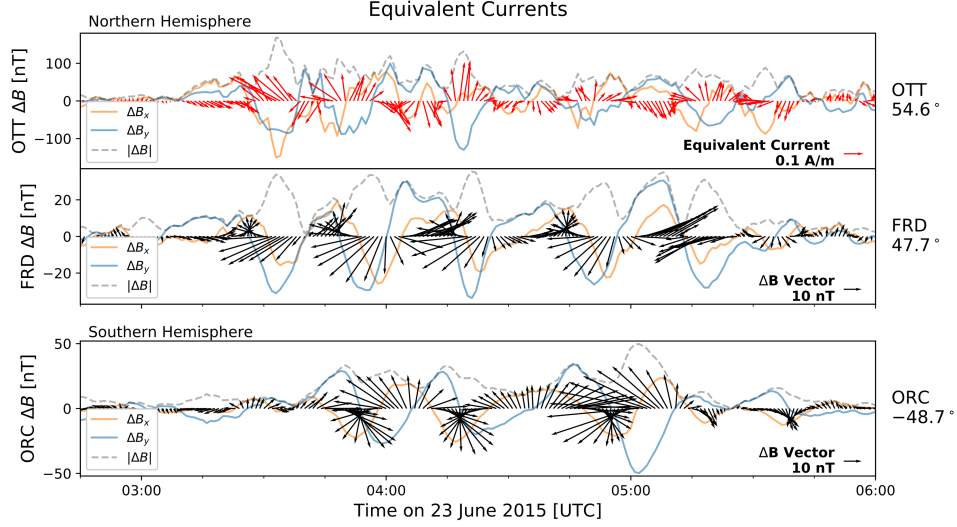


**Figure 5.** Equivalent current vectors for OTT, at the equatorward edge of the aurora, are shown along with the disturbance B-field vectors for FRD and ORC, both at similar latitudes but in opposite hemispheres. Whereas the  $B_x$  component at OTT is affected by the electrojet, the lower latitude sites show a consistent pulsation signature and polarisation.

As mentioned previously, such regular, long period, high amplitude oscillations in GIC driving can cause significant accumulated damage or ageing to equipment – possibly more so than typical higher frequency pulsations. Comparing the roughly two hour period of Ps6 activity (second shaded region in Figure 3) to a similar duration of activity after the SSC, which included the most active part of the main phase (first shaded region in Figure 3), the RMS of the GIC during Ps6 driving exceeded that of the SSC and main phase onset by 10%. In terms of the sum of absolute GIC magnitude for these two periods, the pulsation period had over 20% more exposure. Furthermore, the Ps6 activity is cyclical, with sustained and constant repeated GIC driving possibly stressing transformers more. The nature of the power system response given such driving is part of ongoing research.

Even though the Ps6 event was seen in measured GIC data in the entire TVA network, it has a predominant directionality. Specifically, the dominant D or  $B_y$  component of the B-field drives a stronger north-south E-field that affects north-south nodes (such as PAR) more than nodes with an east-west effective orientation. TVA was not the only network affected – at a substation in a neighbouring network the GIC pulsation peaks were around 25 A. The extent of the geomagnetic disturbance – about 15 degrees in geographic latitude and 30 degrees geographic longitude – means that the entire eastern North America was likely affected, modulated by local ground conductivity conditions. Pulsations are however likely to be part of a geomagnetic storm and occur after the system has already been stressed by the sudden storm impulse and main phase driving, i.e. the largest sustained cumulative stressing comes after the system is already stressed and vulnerable. It is most unlikely that gas bubbles formed in transformer winding insulation during the initial onset of the storm would be reabsorbed by the time of the pulsation activity. During the second stronger period of accumulated driving, further partial discharge could increase ageing and accumulated damage.

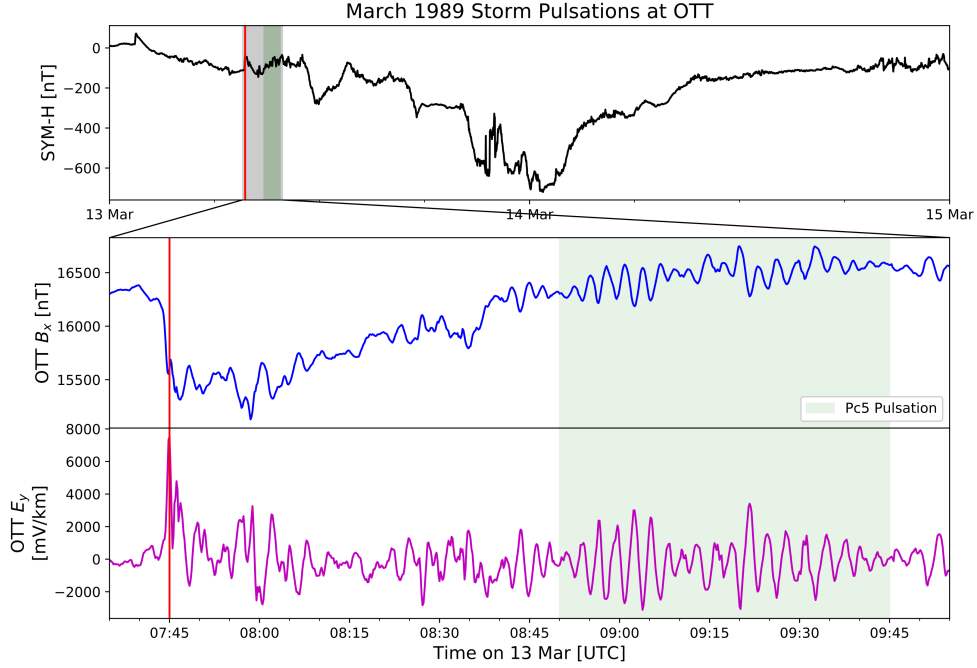


**Figure 6.** Time series of the detected Pc5 pulsations (green shaded region) at OTT during March 1989 storm using the NERC defined benchmark geoelectric field (magenta) (*TPL-007-1: Transmission System Planned Performance for Geomagnetic Disturbance Events*, North American Reliability Corp., 2017.). A red line indicates the time of collapse of the Hydro-Québec network (Boteler, 2019).

### 4.3 Event 3: March 1989 Geomagnetic Storm

Event 3 is included in this analysis specifically because it plays such a critical role in current utility and modelling benchmarking. The March 1989 geomagnetic storm that resulted in the now famous Hydro-Québec blackout (Bolduc, 2002; Boteler, 2019) can probably be regarded as the catalyst for the intense modern study of GICs. In the NERC reliability standard, this storm, along with its B-field and derived E-field profiles at OTT, is used as the regulatory benchmark for utility planning. As stated before, only peak GIC hence driving E-field values are considered in the standard. Figure depicts this event with SYM-H index (top panel) for the entire storm, along with OTT  $B_x$  and derived  $E_y$  profiles. The moment of the Hydro-Québec blackout is indicated by a red line. Specifically highlighted in the interval 07:00 – 10:00 UTC on 13 March 1989 are 6 mHz Pc5 pulsations with significant amplitude for about an hour around 09:00 UTC, embedded in both the geomagnetic and geoelectric fields. Given that these pulsations are fall within the interval of interest of the NERC benchmark storm, modelling efforts should be extended to include the effects of such low-frequency GIC driving in a power system context.

OTT is a high mid-latitude station where Pc5 pulsations are likely to occur, but pulsations were also seen at lower mid-latitudes in Europe (Villante et al., 1990) suggesting the type of global Pc5 event seen during geomagnetically disturbed periods (Pilipenko et al., 2010). Pc5 pulsations are more often associated with the  $B_x$  component of the B-field, and as such the variation would affect the east-west E-field component and east-west networks more. In the case of the Hydro-Québec blackout, it is likely that the second of a series of CMEs coincided with a substorm which resulted in a large eastward

electrojet that knocked out the power system (Boteler, 2019). For the NERC benchmark event these pulsations at OTT result in an oscillating east-west E-field of roughly 2 V/km (4 V/km peak-to-peak) over a sustained period (Figure 6). This E-field level is only 25% of the 8 V/km extreme case for thermal damage (*TPL-007-1: Transmission System Planned Performance for Geomagnetic Disturbance Events*, North American Reliability Corp., 2017.) but may result in significant accumulated damage and control maloperation. The exact nature of such damage due to pulsations in Event 3 is not known since the Hydro-Québec outage happened during the sudden impulse at 07h45 (Boteler, 2019), before either the Pc5 pulsations or the peak of the storm. As alluded to above, if the network had not collapsed but rather been in a stressed state, the pulsation driving may even more effective at introducing damage. The fact the pulsations occurred before the main phase of the superstorm is of interest when compared to the similar Pc5 pulsations in the recovery phase of the 2003 Halloween storm. In the case of the 1989 storm, the Pc5 pulsation period followed the SSC of a high-speed CME, which in turn followed an initial CME that had already disturbed the near-Earth environment (evidenced by the SSC coinciding with a substorm), possibly having similar effects to the 2003 Halloween storm. Multiple CME scenarios are inherently more complex, with subsequent CMEs having faster speeds after their path is cleared by a preceding CME (Boteler, 2019), and possibly triggering intense substorms (Tsurutani et al., 2015). Besides being more complex, these multiple event storms may be more dangerous to power systems than single more extreme events. A power network does not distinguish events and, given its temporal sensitivity, would see the entire period as uninterrupted driving.

## 5 Pulsation appropriate GIC proxies

The time derivative of the disturbed B-field has long been used as a proxy for GIC activity, largely due to its importance in Faraday’s law of induction that drives GICs (Viljanen et al., 2001). A large number of studies have compared the characteristics of GICs and  $dB/dt$  and found agreement (Viljanen, 1997) with direct relations between the maxima of the two quantities possible (Kataoka & Pulkkinen, 2008). A further improvement on the  $dB/dt$  proxy is the use of a rolling maximum of either 1 hour or 3 hours (Trichtchenko & Boteler, 2004) or more recently 30 minutes (Viljanen et al., 2015). These  $dB/dt$  proxies are useful as they do particularly well in resolving the SSC or substorm commencement periods, associated with large GIC values. In the frequency domain, impulses need broadband frequency contributions to be reproduced accurately – including frequencies higher than is typical for geomagnetic variation.

A common misunderstanding is that  $dB/dt$  measured at Earth’s surface drives the E-field which drives GICs. In fact the entire induction loop that stretches deep into the Earth needs to be taken into account, with the result that the Earth modulates the disturbance  $dB/dt$  in the frequency domain and acts as a low-pass filter for this variation (Boteler & Pirjola, 2017). As a direct result, and taking into account that lower B-field frequencies have a larger spectral content than higher frequencies, most of the GIC power sits below 50 mHz (Oyedokun et al., 2020). The spectral peaks of pulsations sit on top of a ‘ $1/f$ ’ slope and this low-pass effect is ultimately why low-frequency pulsations couple to GICs so well.

More specifically, the B-field has a power spectrum (defined as magnitude squared) that follows a  $1/f^m$  relation with frequency, where  $m$  is often between 1 and 2 (Takahashi & Anderson, 1992), but can be higher (Simpson & Bahr, 2005). In the frequency domain,  $dB/dt$  or  $Bdot$  introduces a high-pass filter of  $f$  in relation to the B-field, i.e.  $Bdot(f) = 2\pi i f B(f)$ . The resulting power spectrum in turn follows a  $f^2/f^m$  or  $1/f^{m-2}$  relation with frequency, where  $m-2 \geq 0$ . where Both the E-field and the associated GIC spectra slopes sit between these two values i.e. the E-field and GIC spectra follow a  $1/f^{m*}$  relation where  $0 \leq m-2 < m_* < m$ . Relative to the E-field and GIC spectra, the B-field spectrum has a low-pass response and  $dB/dt$  a high-pass response. Due to the rel-

active responses, a B-field proxy would be biased towards low frequencies and a  $dB/dt$  proxy would be biased towards high frequencies. In case of time domain B-field differencing used to estimate  $dB/dt$ , noise at the sampling rate can effectively drown out signals from low-frequency pulsations. At these low amplitudes, the largest contribution to noise would be instrument noise, with the effect more prominent in less sensitive instruments.

Illustrative of these relations is the homogeneous Earth case, where  $E(f) \propto \sqrt{f}B(f)$  (Cagniard, 1953). The power spectrum of the E-field would follow a  $f/f^m$  or  $1/f^{m-1}$  relation with frequency. For this example let us assume  $m = 2$ , with the B-field power spectrum following a  $1/f^2$  relation with frequency,  $dB/dt$  having a flat frequency response and GICs and the E-field having a  $1/f$  relation. In this scenario let the sampling frequency be 1 Hz and there be Pc5 pulsations of 150 s. For  $dB/dt$ , the ratio of frequency scaling between the pulsation frequency and Nyquist frequency is 1, whereas for the GIC spectrum it would be 75. For that same pulsation signal, the  $dB/dt$  signal would need to be 75 times stronger to be an accurate proxy for the GIC signal. Given longer period pulsations, such as the Ps6 type-disturbances seen at PAR, the effect is even larger. Ultimately, the high-frequency noise can drown out low-frequency pulsation signals. Peaks or spikes on the other hand are broadband driving and are adequately reproduced by  $dB/dt$ . When dealing with 1 minute cadence B-field data, the sampling rate is closer to the frequency of low-frequency pulsations and performs better than the 1 s cadence data, which is becoming more widely available as observatories modernise (Turbitt, 2014). Of course using too low a cadence for the same Pc5 pulsations, such as 5 minutes, will miss the pulsation activity entirely, as seen in Figure 2 with the Pc4 pulsation in 1 minute cadence data at GRS. Ideally, a pulsation effective proxy would have to match the relative weightings of the sampling rate's Nyquist frequency with the narrow-band pulsation's frequency. The proxy would further need to satisfy this condition for multiple pulsation bands.

A possible further manifestation of the high-frequency bias of  $dB/dt$  is possibly seen in cases where the B-field is more closely correlated to GIC than  $dB/dt$  (Watari et al., 2009). As mentioned, the surface  $dB/dt$  field is not a true reflection of the GIC driver and the Earth's conductivity structure needs to be taken into account. A complex conductivity structure can explain the cases where confusion arises to a large degree (Watari et al., 2009; Pirjola, 2010; Pulkkinen et al., 2010). In the more extreme case of the June 2015 storm presented in this paper, we see high correlation between GIC and  $dB/dt$  as well as the B-field during different parts of the storm. As seen in Figure 3, during the low-frequency Ps6 event, the B-field is representative of the GIC profile and shows similar structure in period and phase. In Figure 7, we see that during the broadband SSC of the same storm,  $dB/dt$  is representative of the GIC profile. The B-field intrinsically has lower frequency components compared to  $dB/dt$ , especially at 1 s sampling cadence. During a pulsation interval with a roughly 20 minute period, 1 s cadence  $dB/dt$  cannot reproduce the variation required, as seen in the middle panel of Figure 7. For the impulse during the SSC on the other hand, a higher cadence can better resolve the peak and  $dB/dt$  with its higher frequency content does better. Similar results are seen with other pulsations, such as Pc5's at GRS in Figure 2 where the B-field is representative of GIC. Up to now it has been fortuitous that 1 minute sampling has more spectral weight than 1 s sampling, with the result that 1 minute  $dB/dt$  has been more representative for common pulsations with periods on the order of a few minutes. Given larger disparities between a high sampling rate and low-frequency driving, whatever the Earth conductivity, the high sampling rate alone will not be satisfactorily representative.

In the case of low-frequency driving and the modern standard of 1 s cadence B-field data, instead of  $dB/dt$  a proxy akin to E-field will be much more effective (Marshall et al., 2010, 2011). In the frequency domain, the two components (directional projections)

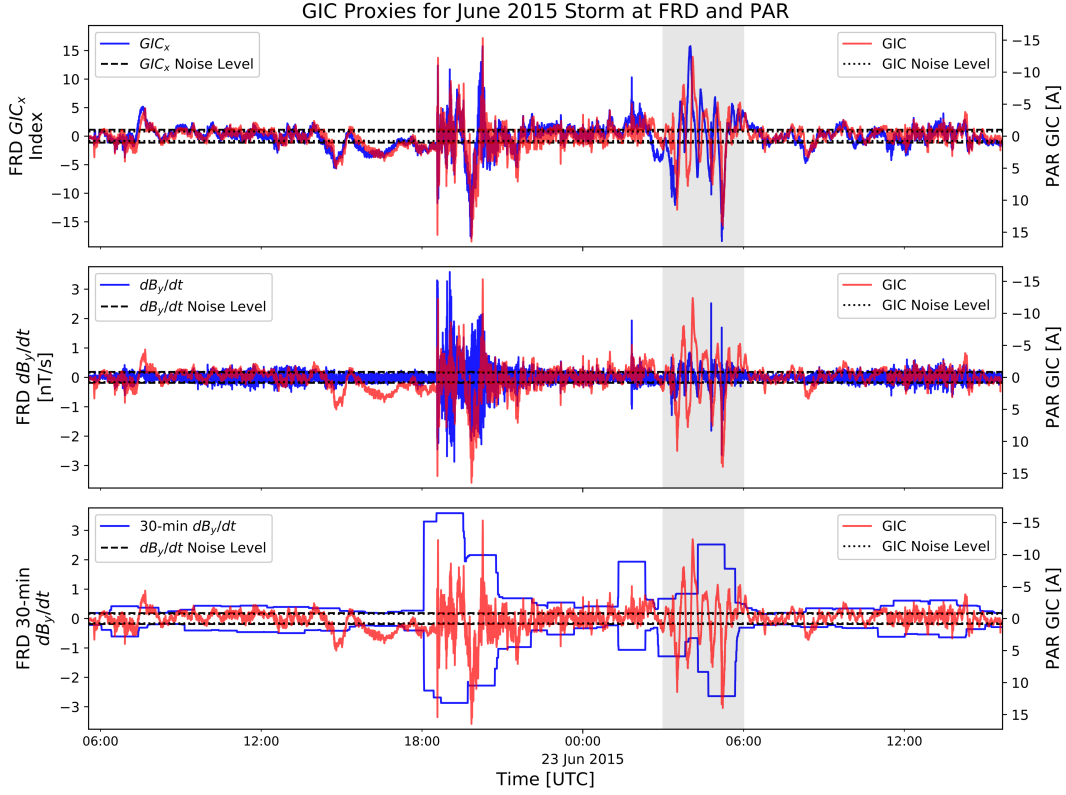


**Figure 7.** GIC frequency weighted proxy  $GIC_x$  at PAR during June 2015 storm that included the Ps6 type disturbance (upper panel). Since the lines at PAR are effectively north-south, only the  $GIC_x$  proxy is shown. Both the Ps6 pulsation, SSC and other low amplitude structures are captured. The time lag in signatures during Ps6 event is due to separation between FRD and PAR given a localized event. Middle panel shows traditional  $dB/dt$  at 1 s cadence which misses the pulsation event and low amplitude structures. Bottom panel shows the often used rolling 30 min  $dB/dt$  envelope which does better but also misses the pulsation event. Dashed black lines indicate 5 sigma from mean noise levels either GIC or proxies.



of the GIC proxy would be,

$$GIC_{x,y}(f) \propto \pm \frac{1}{\sqrt{f}} Bdot_{y,x}(f), \quad (3)$$

where  $Bdot$  refers to  $dB/dt$  and the orthogonality between driving and induced components is explicitly absorbed. The B-field or  $dB/dt$  can be used interchangeably, since they are linked in the frequency domain by  $2\pi if$ .  $dB/dt$  does however have the benefit of being centred about zero and no baseline subtraction is needed when applying the FFT. Taking the inverse FFT gets the resulting proxy for each component in the time domain. A normalised version of the GIC proxy defined by Marshall et al. (2011) can be used to estimate levels of GIC risk (Marshall et al., 2011; Zhang et al., 2016; Tozzi et al., 2019). The focus here is rather on replicating pulsations in a GIC proxy and (3) is applied as is. In Figure 7 only the  $GIC_x$  proxy that is related to the  $B_y$  component is shown as the network is north-south effective at PAR, with GIC axis inverted as before due to network parameter polarity. In all subfigures, the 5 sigma noise level of the parameters during quiet time is indicated with horizontal dashed lines, with overlap in some cases. Any proxy used should aim to characterise signals well when above this level. The  $GIC_{x,y}$  proxy effectively takes into account the low-pass frequency weighting needed to reproduce measured GIC across all frequencies, adhering to where GIC power sits independent of sampling rate and doing significantly better than the other proxies. Although it looks very similar to the derivation of the E-field for a homogeneous Earth it should be stressed that  $GIC_{x,y}$  is just a frequency weighted proxy with no further scaling. In such a way even long period pulsations can be identified with other pulsations and impulses in a single proxy using high cadence data. Standardising the proxy with no further scaling means the proxy is comparable for different events and stations. Ultimately, different events can be characterised using this common proxy for different stations (Marshall et al., 2011; Tozzi et al., 2019), similar to SYM-H, and relative storm strengths quantified across frequencies and conductivity regions in such a way. Taking into account the cumulative proxy is also of interest as it can identify possible degradation risk (Lotz & Danskin, 2017; Moodley & Gaunt, 2017).

## 6 Conclusions

Although pulsations have been acknowledged as sources of GIC driving and are used extensively as signal sources for magnetotelluric sounding (Simpson & Bahr, 2005) in the geophysical step of GIC modelling, the extent of their contribution has often not been recognised, especially at mid-latitudes where population density, and therefore power network coverage, peaks. In this paper pulsation signatures linked to geomagnetic pulsations were identified in measured mid-latitude GIC data during intense and extreme geomagnetic storms. The coupling and amplitude of GIC associated with pulsations is proportional to the period making low-frequency pulsations significant. Given two pulsations of the same amplitude, the longer period pulsation will couple more efficiently and drive larger GICs. As such peak  $dB/dt$  is not the ultimate proxy for GIC-related damage, as efficient coupling during pulsation intervals can occur while  $dB/dt$  is moderate. Using measured data, we've shown that pulsations can drive significant GIC at a mid-latitude network during intense geomagnetic storms. Further statistical analysis using more events is however needed to fully estimate the prevalence and impact of GIC critical pulsations in general.

Specifically, two geomagnetic storms that had low-frequency oscillations in the Pc5 and Ps6 bands were observed to couple to significant measured GICs at mid-latitude locations. A third storm, used for regulatory benchmarking, found similar Pc5 coupling in the derived E-field, which ultimately drives GICs. The characteristics of the two pulsation types seen are very different. Global Pc5 events tend to be associated with superstorms or multiple CME storms and affect the entire globe. The  $B_x$  component of the B-field is dominant and east-west nodes in power networks are more at risk. Larger



amplitude Ps6 events on the other hand are associated with FACs and are not as dependent on storm intensity, although coinciding with geomagnetic storm minimum may make them more effective, with their effects seen in GIC driving at mid-latitudes. These events are also more spatially localised and restricted from the pre-midnight to morning sectors, although they may last a number of hours and have associated drift, making local B-field measurements for GIC modelling necessary. The dominant  $B_y$  component in turn means north-south nodes in power networks are more at risk.

Storm time global Pc5 pulsations were found to generate significant GIC or GIC effective E-fields in the famous superstorms of 1989 and 2003, reaching amplitudes between a quarter and two thirds of those at the SSC for extended periods of over an hour. An intense Ps6-type substorm associated disturbance occurring during the 22–23 June 2015 geomagnetic storm was shown to be a widespread event that covered most of the eastern North America. This event caused GICs of about 10 A at regular 20 minute intervals over a 2 and a half hour period at a mid-latitude station not previously thought to be affected by Ps6 disturbances. The sustained cumulative GIC pulsation driving as measured by RMS over a roughly two hour period exceeded that of a similar two hour period including the SSC and main phase onset by 10%. At higher latitudes or in different networks these effects can possibly be larger, as has been shown in the Kola peninsula (Apatenkov et al., 2020). Ps6 disturbances are a function of magnetosphere dynamics, with the challenging prediction of the magnetotail and substorm environment, along with fine structures in the near-Earth current systems, required for an operational lead time useful to utilities.

From an engineering aspect, both the Pc5 and Ps6 types of pulsations induce significant low-frequency GICs that cannot be modelled accurately using only a dc assumption. For more representative and realistic modelling of the stress to transformers and the power system, a driving ac current with frequencies up to the Pc5 pulsation band (6.7 mHz) is needed. Such modelling is distinctly different to dc modelling and would already be needed if the NERC benchmark profile were applied explicitly, since there is Pc5 driving in the benchmark March 1989 storm. The direct damage caused by pulsations is not the same as that of peak currents, but may contribute to voltage instability, initiate insulation degradation and cause corrosion in pipelines. A further consideration is that pulsation driving typically occurs after the SSC peak GIC and often in the recovery phase when the system is already under stress.

When considering pulsations, the typical  $dB/dt$  proxy widely used no longer describes active periods when the pulsation frequency is significantly different from the sampling frequency of the B-field. This is evident in the June 2015 storm, where a Ps6 pulsation interval with a period of over 20 minutes was not identified in either 1 s cadence  $dB/dt$  or a rolling max window derived from 1 s cadence  $dB/dt$ . A frequency weighted proxy that captures the low-pass filter effect of the Earth’s conductivity on  $dB/dt$  has been shown to capture pulsation activity in multiple bands adequately.

## Acknowledgments

This work was funded in part by a grant from the Open Philanthropy Project (OPP) Fund. The authors acknowledge Eskom and the EPRI Sunburst project for measured GIC data in South Africa and Tennessee Valley Authority (TVA) for GIC data in the USA. These utility datasets are available upon application. The benchmark geomagnetic and geoelectric field profiles for the March 1989 storm are available on the NERC GMD Task Force project webpage, [www.nerc.com/comm/PC/Pages/Geomagnetic-Disturbance-Task-Force-\(GMDTF\)-2013.aspx](http://www.nerc.com/comm/PC/Pages/Geomagnetic-Disturbance-Task-Force-(GMDTF)-2013.aspx). The results presented in this paper rely on data collected at magnetic observatories. We thank the national institutes that support them and INTERMAGNET for promoting high standards of magnetic observatory practice ([www.intermagnet.org](http://www.intermagnet.org)). Raw geomagnetic field data from magnetotelluric field units (RES46 and TNV47), part of the USArray Transportable Array, were used and are avail-

able through the The IRIS Data Management Center (IRISDMC) (doi:10.7914/SN/EM). Data from a legacy pulsation magnetometer operated by SANSa in Sutherland, South Africa, was also used for verification and is further acknowledged. The authors also gratefully acknowledge the SuperMAG (Gjerloev, 2012) collaborators (<http://supermag.jhuapl.edu/info/?page=acknowledgement>) regarding the SML and SMU indices used (Newell & Gjerloev, 2011) and NASA/GSFCs Space Physics Data Facility’s OMNIWeb (or CDAWeb or ftp) service and OMNI data for the SYM-H index and IMF geomagnetic field measurements. All data used to create figures may be downloaded from [ftp://ftp.spacesci.sansa.org.za/pub/slotz/heyns\\_lotz\\_gaunt.202002/](ftp://ftp.spacesci.sansa.org.za/pub/slotz/heyns_lotz_gaunt.202002/). A further thanks goes to the SSUSI team and PI, Dr. Larry Paxton, at JHU/APL (<https://ssusi.jhuapl.edu/>) for the provision of calibrated DMSP/SSUSI auroral radiance data.

## References

- Amm, O., Aksnes, A., Stadsnes, J., Østgaard, N., Vondrak, R., Germany, G., ... Viljanen, A. (2005). Mesoscale ionospheric electrodynamics of omega bands determined from ground-based electromagnetic and satellite optical observations. *Annales Geophysicae*, 23(2), 325–342. doi: 10.5194/angeo-23-325-2005
- Apatenkov, S. V., Pilipenko, V. A., Gordeev, E. I., Viljanen, A., Juusola, L., Belakhovsky, V. B., ... Selivanov, V. N. (2020). Auroral Omega Bands are a Significant Cause of Large Geomagnetically Induced Currents. *Geophysical Research Letters*, 47(6). doi: 10.1029/2019GL086677
- Apatenkov, S. V., Sergeev, V. A., Pirjola, R., & Viljanen, A. (2004). Evaluation of the geometry of ionospheric current systems related to rapid geomagnetic variations. *Annales Geophysicae*, 22(1), 63–72. doi: 10.5194/angeo-22-63-2004
- Balasis, G., Daglis, I. A., Mann, I. R., Papadimitriou, C., Zesta, E., Georgiou, M., ... Tsinganos, K. (2015). Multi-satellite study of the excitation of Pc3 and Pc4-5 ULF waves and their penetration across the plasmopause during the 2003 Halloween superstorm. *Annales Geophysicae*, 33(10), 1237–1252. doi: 10.5194/angeo-33-1237-2015
- Belakhovsky, V., Pilipenko, V., Engebretson, M., Sakharov, Y., & Selivanov, V. (2019). Impulsive disturbances of the geomagnetic field as a cause of induced currents of electric power lines. *Journal of Space Weather and Space Climate*, 9, A18. doi: 10.1051/swsc/2019015
- Bolduc, L. (2002). GIC observations and studies in the Hydro-Québec power system. *Journal of Atmospheric and Solar-Terrestrial Physics*, 64(16), 1793–1802. doi: 10.1016/S1364-6826(02)00128-1
- Borovsky, J. E., & Yakymenko, K. (2017). Substorm occurrence rates, substorm recurrence times, and solar wind structure. *Journal of Geophysical Research: Space Physics*, 122(3), 2973–2998. doi: 10.1002/2016JA023625
- Boteler, D. H. (2015). The Evolution of Québec Earth Models Used to Model Geomagnetically Induced Currents. *IEEE Transactions on Power Delivery*, 30(5), 2171–2178. doi: 10.1109/TPWRD.2014.2379260
- Boteler, D. H. (2019). A 21st Century View of the March 1989 Magnetic Storm. *Space Weather*, 17(10), 1427–1441. doi: 10.1029/2019SW002278
- Boteler, D. H., & Pirjola, R. J. (2017). Modeling geomagnetically induced currents. *Space Weather*, 15(1), 258–276. doi: 10.1002/2016SW001499
- Cagniard, L. (1953). Basic Theory of the Magneto-Telluric Method of Geophysical Prospecting. *GEOPHYSICS*, 18(3), 605–635. doi: 10.1190/1.1437915
- Cheng, C.-C., Mann, I. R., & Baumjohann, W. (2014). Association of consecutive Pi2-Ps6 band pulsations with earthward fast flows in the plasma sheet in response to IMF variations. *Journal of Geophysical Research: Space Physics*, 119(5), 3617–3640. doi: 10.1002/2013JA019275
- Connors, M., Rostoker, G., Sofko, G., McPherron, R. L., & Henderson, M. G. (2003). Ps 6 disturbances: relation to substorms and the auroral oval. *An-*

- nales *Geophysicae*, 21(2), 493–508. doi: 10.5194/angeo-21-493-2003
- de Villiers, J. S., Kosch, M., Yamazaki, Y., & Lotz, S. (2017). Influences of various magnetospheric and ionospheric current systems on geomagnetically induced currents around the world. *Space Weather*, 15(2), 403–417. doi: 10.1002/2016SW001566
- Divett, T., Richardson, G. S., Beggan, C. D., Rodger, C. J., Boteler, D. H., Ingham, M., ... Dalzell, M. (2018). Transformer-Level Modeling of Geomagnetically Induced Currents in New Zealand’s South Island. *Space Weather*, 16(6), 718–735. doi: 10.1029/2018SW001814
- Federal Energy Regulatory Commission: Reliability Standard for Transmission System Planned Performance for Geomagnetic Disturbance Events. Order 830.* (Sep 2016, Washington DC.). <https://www.ferc.gov/whats-new/comm-meet/2016/092216/E-4.pdf>.
- Freeman, M. P., Forsyth, C., & Rae, I. J. (2019). The Influence of Substorms on Extreme Rates of Change of the Surface Horizontal Magnetic Field in the United Kingdom. *Space Weather*, 17(6), 827–844. doi: 10.1029/2018SW002148
- Fukushima, N. (1976). Generalized theorem for no ground magnetic effect of vertical currents connected with Pedersen currents in the uniform-conductivity ionosphere. *Report of Ionosphere and Space Research in Japan*, 30(1-2), 35-40.
- Gaunt, C. T., & Coetzee, G. (2007). Transformer failures in regions incorrectly considered to have low GIC-risk. In *2007 IEEE Lausanne Power Tech* (pp. 807–812). IEEE. doi: 10.1109/PCT.2007.4538419
- Gjerloev, J. W. (2012). The SuperMAG data processing technique. *Journal of Geophysical Research: Space Physics*, 117(A9). doi: 10.1029/2012JA017683
- Gonzalez, W. D., Joselyn, J. A., Kamide, Y., Kroehl, H. W., Rostoker, G., Tsutsumi, B. T., & Vasyliunas, V. M. (1994). What is a geomagnetic storm? *Journal of Geophysical Research*, 99(A4), 5771. doi: 10.1029/93JA02867
- Hejda, P., & Bochníček, J. (2005). Geomagnetically induced pipe-to-soil voltages in the Czech oil pipelines during October-November 2003. *Annales Geophysicae*, 23(9), 3089–3093. doi: 10.5194/angeo-23-3089-2005
- Henderson, M. G., Kepko, L., Spence, H. E., Connors, M., Sigwarth, J. B., Frank, L. A., ... Yumoto, K. (2002). The evolution of north-south aligned auroral forms into auroral torch structures: the generation of omega bands and Ps6 pulsations via flow bursts. In *6th International Conference on Substorms* (pp. 1–6). doi: 10.13140/RG.2.1.4976.9688
- Jankee, P., Chisepo, H., Adebayo, V., Oyedokun, D., & Gaunt, C. T. (2020). Transformer models and meters in MATLAB and PSCAD for GIC and leakage dc studies. In *2020 International SAUPEC/RobMech/PRASA Conference* (pp. 1–6). IEEE. doi: 10.1109/SAUPEC/RobMech/PRASA48453.2020.9041060
- Kappenman, J. G. (2005). An overview of the impulsive geomagnetic field disturbances and power grid impacts associated with the violent Sun-Earth connection events of 29-31 October 2003 and a comparative evaluation with other contemporary storms. *Space Weather*, 3(8). doi: 10.1029/2004SW000128
- Kataoka, R., & Pulkkinen, A. (2008). Geomagnetically induced currents during intense storms driven by coronal mass ejections and corotating interacting regions. *Journal of Geophysical Research: Space Physics*, 113(A3). doi: 10.1029/2007JA012487
- Khawaja, R. H., & Blackburn, T. R. (2009). Impact of high temperature on partial discharges in oil-impregnated insulation. In *2009 Australasian Universities Power Engineering Conference* (p. 1-6). IEEE. Retrieved from <https://ieeexplore.ieee.org/document/5356639>
- Kozyreva, O., Pilipenko, V., Krasnoperov, R., Baddeley, L., Sakharov, Y., & Dobrovolsky, M. (2019). Fine structure of substorm and geomagnetically induced currents. *Annals of Geophysics*, 62. doi: 10.4401/ag-8198

- Le, G., Cai, Z., Wang, H., & Zhu, Y. (2012). Solar cycle distribution of great geomagnetic storms. *Astrophysics and Space Science*, 339(1), 151–156. doi: 10.1007/s10509-011-0960-y
- Lehtinen, M., & Pirjola, R. (1985). Currents produced in earthed conductor networks by geomagnetically-induced electric fields. *Annales Geophysicae*, 3(4), 479–484.
- Lotz, S. I., & Danskin, D. W. (2017). Extreme Value Analysis of Induced Geoelectric Field in South Africa. *Space Weather*, 15(10), 1347–1356. doi: 10.1002/2017SW001662
- Lühr, H., & Schlegel, K. (1994). Combined measurements of EISCAT and the EISCAT magnetometer cross to study  $\Omega$  bands. *Journal of Geophysical Research*, 99(A5), 8951. doi: 10.1029/94JA00487
- Marin, J., Pilipenko, V., Kozyreva, O., Stepanova, M., Engebretson, M., Vega, P., & Zesta, E. (2014). Global Pc5 pulsations during strong magnetic storms: excitation mechanisms and equatorward expansion. *Annales Geophysicae*, 32(4), 319–331. doi: 10.5194/angeo-32-319-2014
- Marshall, R. A., Smith, E. A., Francis, M. J., Waters, C. L., & Sciffer, M. D. (2011). A preliminary risk assessment of the Australian region power network to space weather. *Space Weather*, 9(10), 1–18. doi: 10.1029/2011SW000685
- Marshall, R. A., Waters, C. L., & Sciffer, M. D. (2010). Spectral analysis of pipe-to-soil potentials with variations of the Earth’s magnetic field in the Australian region. *Space Weather*, 8(5). doi: 10.1029/2009SW000553
- McPherron, R. L. (2005). Magnetic Pulsations: Their Sources and Relation to Solar Wind and Geomagnetic Activity. *Surveys in Geophysics*, 26(5), 545–592. doi: 10.1007/s10712-005-1758-7
- Meng, C.-I., & Liou, K. (2004). Substorm timings and timescales: A new aspect. *Space Science Reviews*, 113(1/2), 41–75. doi: 10.1023/B:SPAC.0000042939.88548.68
- Moodley, N., & Gaunt, C. T. (2017). Low Energy Degradation Triangle for power transformer health assessment. *IEEE Transactions on Dielectrics and Electrical Insulation*, 24(1), 639–646. doi: 10.1109/TDEI.2016.006042
- Nakamura, R., Sergeev, V. A., Baumjohann, W., Plaschke, F., Magnes, W., Fischer, D., ... Saito, Y. (2016). Transient, small-scale field-aligned currents in the plasma sheet boundary layer during storm time substorms. *Geophysical Research Letters*, 43(10), 4841–4849. doi: 10.1002/2016GL068768
- Neska, A., Reda, J. T., Neska, M. L., & Sumaruk, Y. P. (2018). On the relevance of source effects in geomagnetic pulsations for induction soundings. *Annales Geophysicae*, 36(2), 337–347. doi: 10.5194/angeo-36-337-2018
- Newell, P. T., & Gjerloev, J. W. (2011). Evaluation of SuperMAG auroral electrojet indices as indicators of substorms and auroral power. *Journal of Geophysical Research: Space Physics*, 116(A12). doi: 10.1029/2011JA016779
- Ngwira, C. M., Habarulema, J., Astafyeva, E., Yizengaw, E., Jonah, O. F., Crowley, G., ... Coffey, V. (2019). Dynamic Response of Ionospheric Plasma Density to the Geomagnetic Storm of 22-23 June 2015. *Journal of Geophysical Research: Space Physics*, 124(8), 7123–7139. doi: 10.1029/2018JA026172
- Ngwira, C. M., McKinnell, L.-A., Cilliers, P. J., Viljanen, A., & Pirjola, R. (2009). Limitations of the modeling of geomagnetically induced currents in the South African power network. *Space Weather*, 7(10). doi: 10.1029/2009SW000478
- Ohtani, S., Zanetti, L. J., Potemra, T. A., Baker, K. B., Ruohoniemi, J. M., & Lui, A. T. Y. (1994). Periodic longitudinal structure of field-aligned currents in the dawn sector: Large-scale meandering of an auroral electrojet. *Geophysical Research Letters*, 21(17), 1879–1882. doi: 10.1029/94GL00703
- Overbye, T. J., Shetye, K. S., Hughes, Y. Z., & Weber, J. D. (2013). Preliminary consideration of voltage stability impacts of geomagnetically induced currents. In *2013 IEEE Power & Energy Society General Meeting* (pp. 1–5). IEEE. doi:

- 10.1109/PESMG.2013.6673068
- Oyedokun, D., Heyns, M., Cilliers, P., & Gaunt, C. (2020). Frequency Components of Geomagnetically Induced Currents for Power System Modelling. In *2020 International SAUPEC/RobMech/PRASA Conference* (pp. 1–6). IEEE. doi: 10.1109/SAUPEC/RobMech/PRASA48453.2020.9041021
- Paxton, L. J., Meng, C.-I., Fountain, G. H., Ogorzalek, B. S., Darlington, E. H., Gary, S. A., ... Smith, B. E. (1992). Special sensor ultraviolet spectrographic imager: An instrument description. In S. Chakrabarti & A. B. Christensen (Eds.), *Instrumentation for Planetary and Terrestrial Atmospheric Remote Sensing* (pp. 2–15). International Society for Optics and Photonics. doi: 10.1117/12.60595
- Paxton, L. J., Meng, C.-I., Fountain, G. H., Ogorzalek, B. S., Darlington, E. H., Gary, S. A., ... Daniell, Jr., R. E. (1993). SSUSI: Horizon-to-horizon and limb-viewing spectrographic imager for remote sensing of environmental parameters. In R. E. Huffman (Ed.), *Ultraviolet Technology IV* (pp. 161–176). International Society for Optics and Photonics. doi: 10.1117/12.140846
- Paxton, L. J., Schaefer, R. K., Zhang, Y., & Kil, H. (2017). Far ultraviolet instrument technology. *Journal of Geophysical Research: Space Physics*, 122(2), 2706–2733. doi: 10.1002/2016JA023578
- Pilipenko, V., Kozyreva, O., Belakhovsky, V., Engebretson, M. J., & Samsonov, S. (2010). Generation of magnetic and particle Pc5 pulsations during the recovery phase of strong magnetic storms. *Proceedings of the Royal Society A: Mathematical, Physical and Engineering Sciences*, 466(2123), 3363–3390. doi: 10.1098/rspa.2010.0079
- Pirjola, R. (2010). Derivation of characteristics of the relation between geomagnetic and geoelectric variation fields from the surface impedance for a two-layer earth. *Earth, Planets and Space*, 62(3), 287–295. doi: 10.5047/eps.2009.09.002
- Potapov, A., Guglielmi, A., Tsegmed, B., & Kultima, J. (2006). Global Pc5 event during 29–31 October 2003 magnetic storm. *Advances in Space Research*, 38(8), 1582–1586. doi: 10.1016/j.asr.2006.05.010
- Pulkkinen, A., & Kataoka, R. (2006). S-transform view of geomagnetically induced currents during geomagnetic superstorms. *Geophysical Research Letters*, 33(12). doi: 10.1029/2006GL025822
- Pulkkinen, A., Kataoka, R., Watari, S., & Ichiki, M. (2010). Modeling geomagnetically induced currents in Hokkaido, Japan. *Advances in Space Research*, 46(9), 1087–1093. doi: 10.1016/j.asr.2010.05.024
- Pulkkinen, A., Lindahl, S., Viljanen, A., & Pirjola, R. (2005). Geomagnetic storm of 29–31 October 2003: Geomagnetically induced currents and their relation to problems in the Swedish high-voltage power transmission system. *Space Weather*, 3(8). doi: 10.1029/2004SW000123
- Pulkkinen, A., Thomson, A., Clarke, E., & McKay, A. (2003). April 2000 geomagnetic storm: ionospheric drivers of large geomagnetically induced currents. *Annales Geophysicae*, 21(3), 709–717. doi: 10.5194/angeo-21-709-2003
- Rostoker, G., & Barichello, J. C. (1980). Seasonal and diurnal variation of Ps 6 magnetic disturbances. *Journal of Geophysical Research: Space Physics*, 85(A1), 161–163. doi: 10.1029/JA085iA01p00161
- Saito, T. (1969). Geomagnetic pulsations. *Space Science Reviews*, 10(3). doi: 10.1007/BF00203620
- Saito, T. (1978). Long-period irregular magnetic pulsation, Pi3. *Space Science Reviews*, 21(4), 211–212. doi: 10.1007/BF00173068
- Sakurai, T., & Tonegawa, Y. (2005). Extreme magnetic field variations during the October 2003 superstorm. *Advances in Polar Upper Atmosphere Research*(19), 21–41.



- Simpson, F., & Bahr, K. (2005). *Practical Magnetotellurics*. Cambridge: Cambridge University Press. doi: 10.1017/CBO9780511614095
- Sithebe, N. S., & Oyedokun, D. T. O. (2019, sep). Impact of GICs on the Voltage Stability Margin of Power Systems. In *2019 IEEE AFRICON* (pp. 1–6). IEEE. doi: 10.1109/AFRICON46755.2019.9133807
- Smith, A. W., Freeman, M. P., Rae, I. J., & Forsyth, C. (2019). The Influence of Sudden Commencements on the Rate of Change of the Surface Horizontal Magnetic Field in the United Kingdom. *Space Weather*, 17(11), 1605–1617. doi: 10.1029/2019SW002281
- Sokolova, E. Y., Kozyreva, O. V., Pilipenko, V. A., Sakharov, Y. A., & Epishkin, D. V. (2019). Space-Weather-Driven Geomagnetic- and Telluric-Field Variability in Northwestern Russia in Correlation with Geoelectrical Structure and Currents Induced in Electric-Power Grids. *Izvestiya, Atmospheric and Oceanic Physics*, 55(11), 1639–1658. doi: 10.1134/S000143381911015X
- Stephenson, J. A. E., & Walker, A. D. M. (2002). HF radar observations of Pc5 ULF pulsations driven by the solar wind. *Geophysical Research Letters*, 29(9), 81–84. doi: 10.1029/2001GL014291
- Takahashi, K., & Anderson, B. J. (1992). Distribution of ULF energy ( $< 80$  mHz) in the inner magnetosphere: A statistical analysis of AMPTE CCE magnetic field data. *Journal of Geophysical Research*, 97(A7), 10751. doi: 10.1029/92JA00328
- Tigere, S., Phaphathisa, L., Folly, K. A., Oyedokun, D. T. O., & Gaunt, C. T. (2018). Power System Voltage Stability in the Presence of GIC-Like Currents. In *2018 IEEE PES/IAS PowerAfrica* (pp. 567–572). IEEE. doi: 10.1109/PowerAfrica.2018.8521066
- Tozzi, R., De Michelis, P., Coco, I., & Giannattasio, F. (2019). A Preliminary Risk Assessment of Geomagnetically Induced Currents over the Italian Territory. *Space Weather*, 17(1), 46–58. doi: 10.1029/2018SW002065
- TPL-007-1: Transmission System Planned Performance for Geomagnetic Disturbance Events*. (North American Reliability Corp., 2017.). <https://www.nerc.com/pa/Stand/Reliability%20Standards/TPL-007-1.pdf>.
- Trichtchenko, L., & Boteler, D. (2004). Modeling Geomagnetically Induced Currents Using Geomagnetic Indices and Data. *IEEE Transactions on Plasma Science*, 32(4), 1459–1467. doi: 10.1109/TPS.2004.830993
- Tsurutani, B. T., Hajra, R., Echer, E., & Gjerloev, J. W. (2015). Extremely intense ( $SML \leq -2500$  nT) substorms: isolated events that are externally triggered? *Annales Geophysicae*, 33(5), 519–524. doi: 10.5194/angeo-33-519-2015
- Turbitt, C. (2014). *INTERMAGNET Technical Note TN6: INTERMAGNET Definitive One-second Data Standard*. [https://intermagnet.org/publications/im\\_tn\\_06\\_v1.0.pdf](https://intermagnet.org/publications/im_tn_06_v1.0.pdf).
- Vanhamäki, H., Kauristie, K., Amm, O., Senior, A., Lummerzheim, D., & Milan, S. (2009). Electrodynamics of an omega-band as deduced from optical and magnetometer data. *Annales Geophysicae*, 27(9), 3367–3385. doi: 10.5194/angeo-27-3367-2009
- Viljanen, A. (1997). The Relation Between Geomagnetic Variations and Their Time Derivatives and Implications for Estimation of Induction Risks. *Geophysical Research Letters*, 24(6), 631–634. doi: 10.1029/97GL00538
- Viljanen, A., Amm, O., & Pirjola, R. (1999). Modeling geomagnetically induced currents during different ionospheric situations. *Journal of Geophysical Research: Space Physics*, 104(A12), 28059–28071. doi: 10.1029/1999JA900337
- Viljanen, A., Nevanlinna, H., Pajunpää, K., & Pulkkinen, A. (2001). Time derivative of the horizontal geomagnetic field as an activity indicator. *Annales Geophysicae*, 19(9), 1107–1118. doi: 10.5194/angeo-19-1107-2001
- Viljanen, A., Pulkkinen, A., Amm, O., Pirjola, R., Korja, T., & BEAR Working Group. (2004). Fast computation of the geoelectric field using the method of

- elementary current systems and planar Earth models. *Annales Geophysicae*, 22(1), 101–113. doi: 10.5194/angeo-22-101-2004
- Viljanen, A., Wintoft, P., & Wik, M. (2015). Regional estimation of geomagnetically induced currents based on the local magnetic or electric field. *Journal of Space Weather and Space Climate*, 5, A24. doi: 10.1051/swsc/2015022
- Villante, U., Vellante, M., de Lauretis, M., Meloni, A., & Palangio, P. (1990). The strong geomagnetic storm of March 13, 1989 - An analysis at a low latitude station. *Annales Geophysicae*, 8(5), 337–342.
- Walker, A. D. M. (2005). Excitation of field line resonances by sources outside the magnetosphere. *Annales Geophysicae*, 23(10), 3375–3388. doi: 10.5194/angeo-23-3375-2005
- Wanliss, J. A., & Showalter, K. M. (2006). High-resolution global storm index: Dst versus SYM-H. *Journal of Geophysical Research*, 111(A2), A02202. doi: 10.1029/2005JA011034
- Watari, S., Kunitake, M., Kitamura, K., Hori, T., Kikuchi, T., Shiokawa, K., ... Tsuneta, Y. (2009). Measurements of geomagnetically induced current in a power grid in Hokkaido, Japan. *Space Weather*, 7(3). doi: 10.1029/2008SW000417
- Wild, J. A., Woodfield, E. E., Donovan, E., Fear, R. C., Grocott, A., Lester, M., ... Björnsson, G. (2011). Midnight sector observations of auroral omega bands. *Journal of Geophysical Research: Space Physics*, 116(A5), 1–20. doi: 10.1029/2010JA015874
- Wild, J. A., Yeoman, T. K., Eglitis, P., & Opgenoorth, H. J. (2000). Multi-instrument observations of the electric and magnetic field structure of omega bands. *Annales Geophysicae*, 18(1), 99–110. doi: 10.1007/s00585-000-0099-6
- Yagova, N. V., Pilipenko, V. A., Fedorov, E. N., Lhamdondog, A. D., & Gusev, Y. P. (2018). Geomagnetically Induced Currents and Space Weather: Pi3 Pulsations and Extreme Values of Time Derivatives of the Geomagnetic Field's Horizontal Components. *Izvestiya, Physics of the Solid Earth*, 54(5), 749–763. doi: 10.1134/S1069351318050130
- Zhang, J. J., Wang, C., Sun, T. R., & Liu, Y. D. (2016). Risk assessment of the extreme interplanetary shock of 23 July 2012 on low-latitude power networks. *Space Weather*, 14(3), 259–270. doi: 10.1002/2015SW001347
- Zheng, K., Trichtchenko, L., Pirjola, R., & Liu, L.-G. (2013). Effects of Geophysical Parameters on GIC Illustrated by Benchmark Network Modeling. *IEEE Transactions on Power Delivery*, 28(2), 1183–1191. doi: 10.1109/TPWRD.2013.2249119